Vibration isolation performance enhancement using hybrid nonlinear inertial and stiffness elements

Wei Dai [1], Baiyang Shi [2], Jian Yang[3]*, Xiang Zhu [1], Tianyun Li [1]

[1] *School of Naval Architecture & Ocean Engineering, Huazhong University of Science and Technology, Wuhan 430074, P.R. China.*

[2] *Department of Engineering Design and Mathematics, University of the West of England, Bristol BS16 1QY, United Kingdom.*

[3] *Faculty of Science and Engineering, University of Nottingham Ningbo China, Ningbo 315100, P.R. China.*

*e-mail address: *jian.yang@nottingham.edu.cn*

Abstract

Purpose To suppress the low-frequency vibration of dynamic systems such as underwater vehicles, this research proposes a novel geometrically nonlinear vibration isolator using hybrid nonlinear inertial and stiffness elements.

Methods A spring and an inerter are integrated together into a 4-rod linkage structure to form geometric nonlinearity. The performance of isolator under force or base-motion excitation is analysed. The performance of the proposed isolator in a flexible base structure simulating vibration isolation in ships is also considered. The transmissibilities and vibrational energy transfer are taken to evaluate the effectiveness of isolation.

Results The results demonstrate better performance in low-frequency vibration isolation comparing to conventional linear isolator. The combined use of spring and inerter in the linkage mechanism can create a frequency band of ultra-low transmissibility and energy flow at low frequencies.

Conclusion Structural parameters of the proposed hybrid nonlinear element can be designed to alter the dynamic characteristic of the nonlinear isolator to attenuate low-frequency vibration transmission. The proposed nonlinear isolator demonstrates a strong potential for application in naval architecture.

Keywords: geometric nonlinearity; vibration power flow; vibration isolator; inerter; nonlinear spring

1. Introduction

Vibration of the dynamic systems in vessels such as engines and pumps can be transmitted via the mounting base to the wet surface and cause acoustic emission [1]. Considering the reliability, passive vibration isolators are commonly used in vessels to attenuate vibrations from main engines and auxiliaries to the hull [2]. The excessive low-frequency line-spectrum of the underwater vehicle can significantly affect its acoustic stealth performance and harm the creatures in the ocean [3]. Suppression of low-frequency vibration is challenging in the design of vibration isolators of underwater vehicle [4]. It is well-documented that the effective isolation band of a linear isolator starts when the excitation frequency is $\sqrt{2}$ times of the natural frequency of the system [5, 6]. The stiffness of the linear isolator has to be small to isolate low frequency vibration [7], which will affect the load-supporting capability and increase the amplitude of dynamic displacement [8, 9].

To overcome this limitation and improve vibration isolation performance, many recent research interests have focused on the development of vibration isolators exploiting nonlinear elements for performance enhancement [10]. A negative stiffness mechanism (NSM) in parallel with a conventional spring-damper isolator has been studied to reduce the dynamic stiffness of the system [11]. The static deflection of the isolator can be kept small while the resonant frequency is reduced [12-15]. When the system parameters are set at specific values, nonlinear isolators can exhibit quasi-zero-stiffness (QZS) characteristic [16]. Alabuzhev et al. [17] proposed such an isolator consisting of a spring-damper structure and compressed oblique springs. The oblique springs generate the negative stiffness to create a low total dynamic stiffness. In recent years, different configurations of QZS mechanisms have been developed to create the negative stiffness effect [18-21], including beam buckling [22], truss-spring-based structure [23], circular ring [24], QZS isolator with displacement constraints [25] and X-shaped structures [26-30]. Ji et al. [31] reviewed different designs of origami-based structures exhibiting negative stiffness for vibration control. The foldability, multistability and tuneable stiffness characteristics of origami-based structures can be applied to achieve desired vibration isolation performance. Yan et al. [32, 33] examined the transmissibility of a novel lever-type isolator consisting magnetic spring. An et al. [34] investigated the dynamics of a pneumatic QZS isolator having a mistuned mass. Dai et al. [35] proposed a geometrically nonlinear isolator by embedding a spring into a linkage mechanism. It was found that the proposed structure can broaden the effective bandwidth, compared with conventional linear isolators, and reduce the peak value at the vicinity of the resonance. Investigations of various nonlinear isolators have demonstrated the benefits of exploiting nonlinear elements and geometric nonlinearities in vibration suppression.

Many previous studies have focused on nonlinearities by varying the structural stiffness and damping while keeping the mass (i.e., inertial term) constant [36]. Some researchers used lever-type structure to increase the effective mass to lower the natural frequency [37]. The recently proposed inerter device can provide inertial coupling between subsystems (e.g., rack pinion and ball screw) of an integrated structure, so the resulting inertance can be much greater than its physical mass [38]. In view of this, inerter-based vibration isolation/absorption has been a popular research topic and has been employed in various engineering applications [39, 40], including suspension systems [41], aircraft landing gear [42], cables [43] and buildings [44, 45]. However, studies on the inerter-based nonlinear vibration isolator are still lacking. Shi et al. [46] used an inerter in a linkage mechanism and found that the geometric nonlinear inerter device can assist vibration isolation. It is suggested that the nonlinear inertial force can be obtained by embedding inerter in a geometric nonlinear element, which can enhance the isolation performance. Moreover, considering the advantages of spring-based NSM and nonlinear inerter structure. It is interesting to use a hybrid nonlinear inertial and stiffness element in the nonlinear isolator design for further enhancement. However, research on the combined use of nonlinear spring and inerter in nonlinear vibration isolator is rare.

In this study, a hybrid nonlinear inertial and stiffness element is proposed. An inerter and a spring are integrated into a four-bar linkage mechanism. The isolation performance of the geometrically nonlinear isolator is investigated. In addition to the dynamic analysis of a single degree-of-freedom (SDOF) system, the dynamics and performance evaluation of a two degree-of-freedom (2DOF) system representing vibrating equipment mounted on a flexible base is also conducted. The harmonic balance method (HBM) is applied to determine the system response, and the Runge-Kutta method (RKM) is employed as a numerical cross-verification. To understand the mechanism of vibration transmission, vibration power flow indices are used to assess the energy transmission behaviour [47]. The vibrational energy flow has been widely accepted in the quantification of vibration transmission in linear and nonlinear systems [48, 49]. For the rest of the paper, a mathematical model of the hybrid nonlinear element is provided in Section 2. Modelling, formulation and examination of the hybrid nonlinear element in SDOF systems are presented in Section 3. The 2DOF nonlinear isolation system having a flexible base is discussed in Section 4, followed by conclusions.

2. Hybrid nonlinear element with spring and inerter configured in linkage mechanism

Figure 1 shows the model of hybrid nonlinear inertial and stiffness element (NISE), which is configured by inserting a spring of k_{h} and an inerter of b_{h} horizontally in a 4-rod linkage mechanism. The rigid and massless rods with the same length of l_{rod} are connected at four terminals. Terminal B is the connection point to the foundation while terminal A is the load point for equipment mass. The linear spring and the inerter are parallelly hinged to the joint points C and D. The NISE can either be compressed and stretched in the vertical direction.

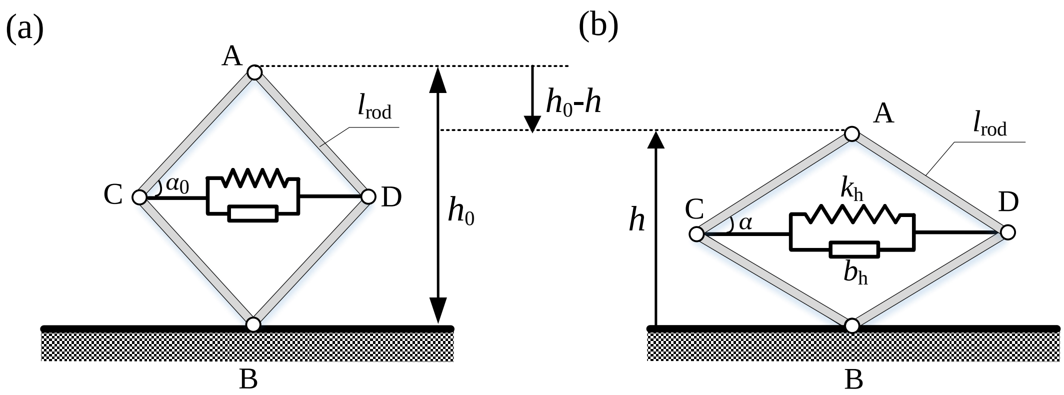

Fig. 1 The model of hybrid nonlinear inertial and stiffness element (NISE) at (a) original un-stretched position and (b) certain position under compression.

Figure 1(a) shows the NISE with the spring un-stretched while Fig. 1(b) shows a certain position of NISE under compression. The original height of NISE is h_0 and the original angle between AC and CD is α_0, as shown in Fig. 1(a). At certain position in Fig. 1(b), the height of NISE becomes h and the angle between AC and CD changes to α with $0 < \alpha < 90°$. It is noted that in the isolator models considered in the current paper, the inerter is considered to be ideal with negligible physical mass as the inertance to physical mass ratio of an inerter can be very high [44].

According to the geometric relation at certain position in Fig. 1(b), the distance relationships are obtained as

$$h = 2l_{\mathrm{rod}} \sin\alpha, \quad d_{\mathrm{CD}} = 2l_{\mathrm{rod}} \cos\alpha = \sqrt{4l_{\mathrm{rod}}^2 - h^2}, \tag{1a}$$

where d_{CD} is the terminal distances of horizontal spring and inerter, i.e., the distance of C and D. Therefore, the relationships of velocity and acceleration are then derived as

$$\dot{h} = 2l_{\mathrm{rod}}\dot{\alpha}\cos\alpha, \quad \ddot{h} = 2l_{\mathrm{rod}}(\ddot{\alpha}\cos\alpha - \dot{\alpha}^2\sin\alpha), \tag{2a, 2b}$$

$$\dot{d}_{\mathrm{CD}} = -2l_{\mathrm{rod}}\dot{\alpha}\sin\alpha, \quad \ddot{d}_{\mathrm{CD}} = -2l_{\mathrm{rod}}(\ddot{\alpha}\sin\alpha + \dot{\alpha}^2\cos\alpha). \tag{2c, 2d}$$

Note that the restoring force of the spring and the inertance force by the inerter depend on the deflection δ_{CD} of spring and relative acceleration $\ddot{d}_{\mathrm{CD}}$ between two terminals of the inerter, respectively. Assuming that the original un-stretched spring length is l_{s}. When terminal A is moving upwards and the NISE is under tension, the spring force and inerter force are

$$f_{\mathrm{spring}} = k_{\mathrm{h}}\delta_{\mathrm{CD}} = k_{\mathrm{h}}(l_{\mathrm{s}} - 2l_{\mathrm{rod}}\cos\alpha), \tag{3a}$$

$$f_{\mathrm{inerter}} = b_{\mathrm{h}}\ddot{d}_{\mathrm{CD}} = 2b_{\mathrm{h}}l_{\mathrm{rod}}(\ddot{\alpha}\sin\alpha + \dot{\alpha}^2\cos\alpha), \tag{3b}$$

respectively. Based on the force equilibrium condition, the downward restoring force of NISE applied to terminal A is

$$f_{\mathrm{NISE}}(\alpha) = \frac{\sin\alpha}{\cos\alpha}(f_{\mathrm{spring}} + f_{\mathrm{inerter}}) = k_{\mathrm{h}}\left(l_{\mathrm{s}}\frac{\sin\alpha}{\cos\alpha} - 2l_{\mathrm{rod}}\sin\alpha\right) + 2b_{\mathrm{h}}l_{\mathrm{rod}}\left(\frac{\ddot{\alpha}\sin^2\alpha}{\cos\alpha} + \dot{\alpha}^2\sin\alpha\right). \tag{4}$$

Using the relation between angle α and element height h in Eq. (1a), the Eq. (4) can be transformed as

$$f_{\mathrm{NISE}}(h, \dot{h}, \ddot{h}) = k_{\mathrm{h}}h\left(\frac{l_{\mathrm{s}}}{\sqrt{4l_{\mathrm{rod}}^2 - h^2}} - 1\right) + b_{\mathrm{h}}\left(\frac{\ddot{h}h^2}{4l_{\mathrm{rod}}^2 - h^2} + \frac{4l_{\mathrm{rod}}^2 h\dot{h}^2}{(4l_{\mathrm{rod}}^2 - h^2)^2}\right). \tag{5}$$

3. NISE vibration isolator in SDOF system

3.1 System modelling

This section illustrates the NISE embedded in a SDOF isolation system subjected to force or displacement excitation. The dynamic modelling and the linearized natural frequency as well as dynamic stiffness characteristics of the system are presented.

3.1.1 SDOF system under force excitation

Figure 2 shows the SDOF isolator model with NISE under force excitation. The isolated equipment has a mass of m_1 and hence the gravity of the mass is $m_1 g$. Here g is the gravitational coefficient. The displacement response of the mass is defined as x_1. The harmonic unbalanced force $f_0\mathrm{e}^{\mathrm{i}\omega t}$ induced by the operation of the equipment is considered as the excitation source. The nonlinear isolator is formed by spring k_1, damper c_1 and NISE with terminal B fixed to the ground. It is defined that when the equipment mass is not installed on the nonlinear isolator, the spring k_1 is unstretched and the length is l_{s1}. After adding the equipment mass to the nonlinear isolator, the NISE is compressed and the height h becomes $h = h_1$, which is set as the equilibrium point of the nonlinear isolator of $x_1 = 0$.

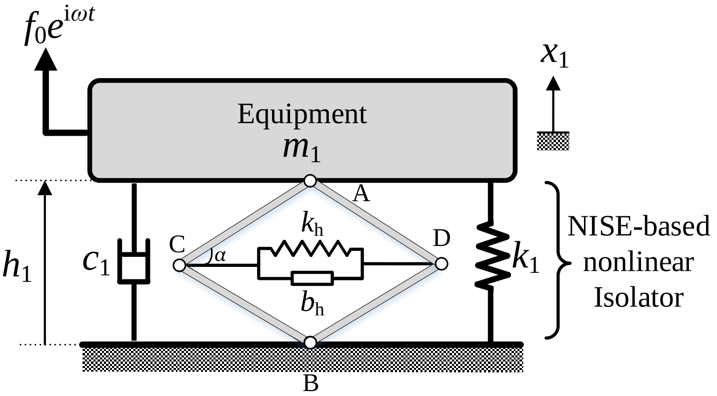

Fig. 2 A SDOF nonlinear isolator model with force excitation

The governing equation is expressed as

$$m_1\ddot{x}_1 + c_1\dot{x}_1 + k_1 x_1 + f_{\mathrm{NISE}}(h,\dot{h},\ddot{h}) + m_1 g = f_0 \mathrm{e}^{\mathrm{i}\omega t}, \tag{6}$$

where the force of NISE is obtained by a substitution of $h = h_1 + x_1$ into Eq. (5):

$$f_{\mathrm{NISE}}(h,\dot{h},\ddot{h}) = k_{\mathrm{h}}(h_1 + x_1)\left(\frac{l_{\mathrm{s}}}{\sqrt{4l_{\mathrm{rod}}^2-(h_1+x_1)^2}} - 1\right) + b_{\mathrm{h}}\left(\frac{(h_1+x_1)^2\ddot{x}_1}{4l_{\mathrm{rod}}^2-(h_1+x_1)^2} + \frac{4l_{\mathrm{rod}}^2(h_1+x_1)\dot{x}_1^2}{\left(4l_{\mathrm{rod}}^2-(h_1+x_1)^2\right)^2}\right). \tag{7}$$

It is noted that when the equipment is installed and the mass reaches the static equilibrium at $h = h_1$, the gravity of the system $m_1 g$ is balanced by the static restoring force $f_{\mathrm{NISE\_static}}$ of NISE with $f_{\mathrm{NISE\_static}} = f_{\mathrm{NISE}}(h_1)$ and static restoring force $f_{\mathrm{k1\_static}}$ of the vertical linear spring at $h = h_1$ with $f_{\mathrm{k1\_static}} = k_1(l_{s1} - h_1)$, we have

$$m_1 g - f_{\mathrm{k1\_static}} - f_{\mathrm{NISE\_static}} = k_1(h_1 - l_{s1}) - k_{\mathrm{h}} h_1\left(\frac{l_{\mathrm{s}}}{\sqrt{4l_{\mathrm{rod}}^2-h_1^2}} - 1\right) + m_1 g = 0. \tag{8}$$

Here parameters are defined

$$\omega_1 = \sqrt{\frac{k_1}{m_1}},\quad \zeta_1 = \frac{c_1}{2m_1\omega_1},\quad F_0 = \frac{f_0}{2k_1 l_{\mathrm{rod}}},\quad \Omega = \frac{\omega}{\omega_1},\quad \tau = \omega_1 t,\quad X_1 = \frac{x_1}{2l_{\mathrm{rod}}}, \tag{9}$$

$$H = \frac{h}{2l_{\mathrm{rod}}},\quad L_{\mathrm{s}} = \frac{l_{\mathrm{s}}}{2l_{\mathrm{rod}}},\quad \lambda_{\mathrm{k}} = \frac{k_{\mathrm{h}}}{k_1},\quad \lambda_{\mathrm{b}} = \frac{b_{\mathrm{h}}}{m_1},\quad H_1 = \frac{h_1}{2l_{\mathrm{rod}}} \tag{10}$$

where ω_1 represents the linearized resonant frequency, ζ_1 marks the damping coefficient, F_0 denotes the amplitude of excitation force, while Ω and τ are the corresponding frequency and time, respectively. X_1 is the response displacement. H is the non-dimensional height of the NISE. L_{s} is the dimensionless unstretched horizontal spring length. λ_{k} is the stiffness coefficient of the horizontal spring. λ_{b} is the inertance coefficient. H_1 is the dimensionless static equilibrium height of the NISE.

Therefore, the Eq. (6) can be nondimensionalized as

$$X_1'' + X_1 + 2\zeta_1 X_1' + F_{\mathrm{NISE}}(H, H', H'') + \frac{m_1 g}{2k_1 l_{\mathrm{rod}}} = F_0 \mathrm{e}^{\mathrm{i}\Omega\tau}, \tag{11}$$

where

$$F_{\mathrm{NISE}}(H, H', H'') = \lambda_{\mathrm{k}}(H_1 + X_1)\left(\frac{L_{\mathrm{s}}}{\sqrt{1-(H_1+X_1)^2}} - 1\right) + \lambda_{\mathrm{b}}\left(\frac{X_1''(X_1+H_1)^2}{1-(X_1+H_1)^2} + \frac{X_1'^2(X_1+H_1)}{(1-(X_1+H_1)^2)^2}\right). \tag{12}$$

According to Eqs. (11) and (12), a negative stiffness could be obtained when $L_{\mathrm{h}}/\sqrt{1-H_1^2} - 1 < 0$. Hence the value of $(L_{\mathrm{h}}^2 + D_1^2)$ should be set less than 1.

By using a second order Taylor expansion, the approximated dynamic force $F_{\mathrm{NISE}}(H, H', H'')$ of the NISE in Eq. (12) can be obtained as

$$F_{\mathrm{NISE}} \approx \lambda_{\mathrm{k}}(\kappa_0 + \kappa X_1) + \lambda_{\mathrm{b}}(X_1'^2 B(X_1) + X_1'' A(X_1)) \tag{13}$$

where

$$\kappa_0 = \left(L_{\mathrm{s}}/\sqrt{1-{H_1}^2} - 1\right)H_1, \quad \kappa = \left({H_1}^2 - 1 + L_{\mathrm{s}}/\sqrt{1-{H_1}^2}\right)\Big/\left(1-{H_1}^2\right), \tag{14}$$

$$A(X_1) = \frac{H_1^2}{1-H_1^2} + \frac{2H_1}{(1-H_1^2)^2}X_1 + \frac{1+3H_1^2}{(1-H_1^2)^3}X_1^2\,, \;\; B(X_1) = \frac{H_1}{(1-H_1^2)^2} + \frac{1+3H_1^2}{(1-H_1^2)^3}X_1 + \frac{6H_1(1+H_1^2)}{(1-H_1^2)^4}X_1^2. \tag{15}$$

Equation (11) is linearized as

$$X_1'' + X_1 + 2\zeta_1 X_1' + \lambda_{\mathrm{k}}(\kappa_0 + \kappa X_1) + \lambda_{\mathrm{b}}(X_1'^2 B(X_1) + X_1'' A(X_1)) = F_0 \mathrm{e}^{\mathrm{i}\Omega\tau}. \tag{16}$$

The linearized resonant frequency is approximated as

$$\Omega_{\mathrm{Linearized}} = \sqrt{\frac{\lambda_{\mathrm{k}}\kappa + 1}{1 + \lambda_{\mathrm{b}}\epsilon_1}}, \tag{17}$$

where $\epsilon_1 = \frac{H_1^2}{1-H_1^2}$. The linearized stiffness is

$$K_{\mathrm{L}} = \lambda_{\mathrm{k}}\kappa + 1. \tag{18}$$

It can be found from Eqs. (17) and (18) that, increasing the inertance ratio can lower the value of $\Omega_{\mathrm{Linearized}}$. Moreover, K_{L} can be reduced to a small value approaching zero by adjusting the value of κ to be negative. This characteristic can be applied to enhance isolation performance at low frequencies.

Figure 3 shows $\Omega_{\mathrm{Linearized}}$ changing with four design parameters of NISE. In Fig. 3(a) and 3(b), the effects of the stiffness ratio λ_{k} and the inertance-mass ratio λ_{b} on $\Omega_{\mathrm{Linearized}}$ are examined. The other design parameters of NISE are set as $L_{\mathrm{s}} = H_1 = 0.5$. It is shown that the increase of λ_{k} or λ_{b} can reduce the value of $\Omega_{\mathrm{Linearized}}$. The reason can be found from Eq. (17) that the linearized natural frequency $\Omega_{\mathrm{Linearized}}$ depends on the value of stiffness ratio λ_{k} and the inertance ratio λ_{b}. In Fig. 3(c) and 3(d), the influence of original spring length L_{s} and static equilibrium height H_1 on $\Omega_{\mathrm{Linearized}}$ is investigated. The other parameters are fixed as $\lambda_k = 2$ and $\lambda_{\mathrm{b}} = 3$. It can be found that a smaller value of L_{s} or H_1 can also reduce the linearized natural frequency. This is due to the relationship between $\Omega_{\mathrm{Linearized}}$ and κ and ϵ_1 from Eq. (17). ϵ_1 is decided by the dimensionless static equilibrium height H_1 of the NISE while κ is related to the dimensionless unstretched horizontal spring length L_{s}. Fig. 3 shows that the inclusion of NISE can improve the low-frequency isolation performance.

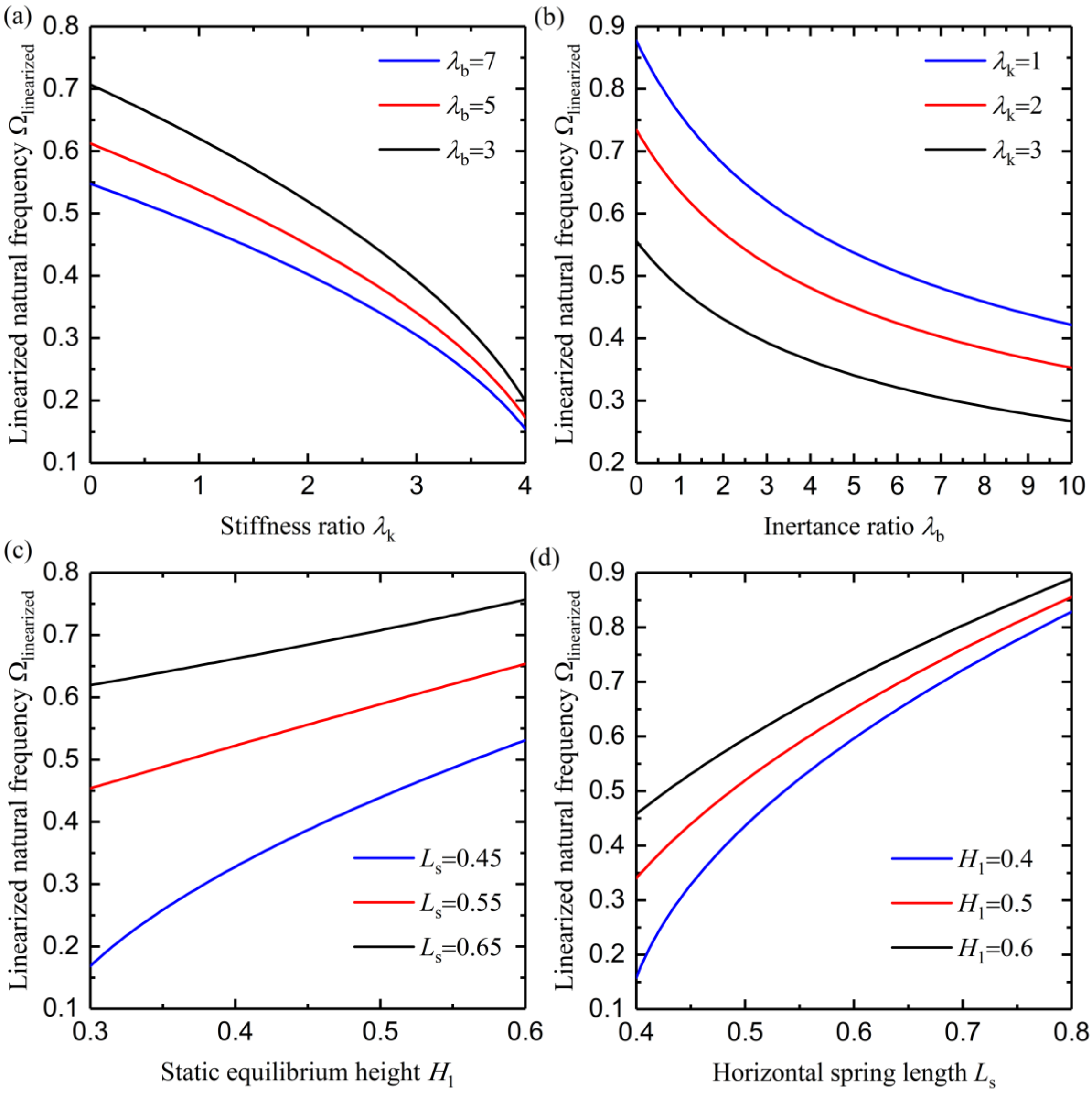

Fig. 3 Linearized resonant frequency of NISE-based SDOF isolator under the influence of (a) stiffness ratio λ_{k}, (b) inertance λ_{b}, (c) static equilibrium height H_1, and (d) horizontal spring length L_{s}. System parameters for (a) and (b): $L_{\mathrm{s}} = 0.5, H_1 = 0.5$; for (c) and (d): $\lambda_{\mathrm{k}} = 2, \lambda_{\mathrm{b}} = 3$

3.1.2 SDOF system under base motion excitation

In this subsection, the NISE is applied for isolating sensitive equipment from the vibration of the foundation shown in Fig. 4. Here the base excitation of $z_0 e^{\mathrm{i}\omega t}$ is considered. Terminal B of the NISE is mounted on the foundation while terminal A is connected to the mass m_1. The static equilibrium is reached at $h = h_1$ after loading, which is set as the reference point of response with $x_1 = 0$.

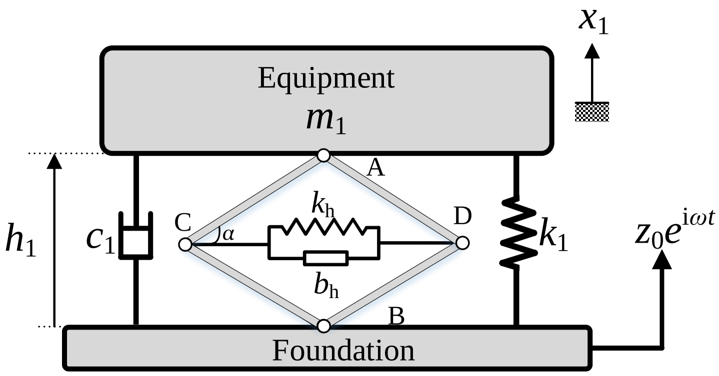

Fig. 4 Model of nonlinear isolation system with NISE under base excitation

Note that the height h of the NISE is $h = h_1 + x_1 - z$, hence the governing equation is expressed as

$$m_1\ddot{x}_1 + c_1(\dot{x}_1 - \dot{z}) + k_1(x_1 - z) + f_{\mathrm{NISE}}(h, \dot{h}, \ddot{h}) + m_1 g = 0, \tag{19}$$

where

$$f_{\mathrm{NISE}}(h, \dot{h}, \ddot{h}) = k_{\mathrm{h}}(h_1 + x_1 - z)\left(\frac{l_{\mathrm{s}}}{\sqrt{4l_{\mathrm{rod}}^2 - (h_1+x_1-z)^2}} - 1\right) + b_{\mathrm{h}}\left(\frac{(h_1+x_1-z)^2(\ddot{x}_1-\ddot{z})}{4l_{\mathrm{rod}}^2-(h_1+x_1-z)^2} + \frac{4l_{\mathrm{rod}}^2(h_1+x_1-z)(\dot{x}_1-\dot{z})^2}{\left(4l_{\mathrm{rod}}^2-(h_1+x_1-z)^2\right)^2}\right). \tag{20}$$

Here the non-dimensional parameters of displacement amplitude $Z_0 = z_0/(2l_{\mathrm{rod}})$ and $Z = Z_0\mathrm{e}^{\mathrm{i}\Omega\tau}$ are introduced. Recalling that at static equilibrium, the gravity of the equipment mass $m_1 g$ is balanced by the static restoring force $f_{\mathrm{NISE\_static}}$ of the NISE and the static restoring force $f_{\mathrm{k1\_static}}$ of the vertical spring. The Eq. (19) is transformed to the dimensionless form as

$$X_1'' + X_1 - Z + 2\zeta_1 X_1' - 2\zeta_1 Z' + F_{\mathrm{NISE}}(H, H', H'') + \frac{m_1 g}{2k_1 l_{\mathrm{rod}}} = 0, \tag{21}$$

where

$$F_{\mathrm{NISE}}(H, H', H'') = \lambda_{\mathrm{k}}(H_1 - Z + X_1)\left(\frac{L_{\mathrm{s}}}{\sqrt{1-(H_1-Z+X_1)^2}} - 1\right) + \lambda_{\mathrm{b}}\left(\frac{(X_1''-Z'')(X_1-Z+H_1)^2}{1-(X_1-Z+H_1)^2} + \frac{(X_1'-Z')^2(X_1+H_1-Z)}{(1-(X_1-Z+H_1)^2)^2}\right). \tag{22}$$

3.2 Assessment of the SDOF isolation system

In solution determination of nonlinear governing equations of Eqs. (11) and (21), both the numerical time-marching method, i.e., the fourth order RKM, and the HBM with alternating frequency time technique (HBM-AFT) are employed [50, 51]. The procedures of HBM-AFT method are illustrated briefly below.

By an approximation of the response and the nonlinear dynamic force of NISE using a N order Fourier series, we have

$$X_1 = \sum_{n=0}^{N} \widetilde{W}_{(1,n)}\, \mathrm{e}^{in\Omega\tau}, \qquad F_{\mathrm{NISE\_dynamic}}(H, H', H'') = \sum_{n=0}^{N} \tilde{Q}_n\, \mathrm{e}^{in\Omega\tau}, \tag{23}$$

where $F_{\mathrm{NISE\_dynamic}} = F_{\mathrm{NISE}}(H, H', H'') - F_{\mathrm{NISE\_static}}(H_1)$, $\widetilde{W}_{(1,n)}$ and $\tilde{Q}_n$ are the n-th order Fourier coefficients with $0 \le n \le N$. The corresponding velocity and acceleration response of the mass are $X_1' = \sum_{n=0}^{N} in\Omega \widetilde{W}_{(1,n)}\, \mathrm{e}^{in\Omega\tau}$ and $X_1'' = -\sum_{n=0}^{N} (n\Omega)^2 \widetilde{W}_{(1,n)}\, \mathrm{e}^{in\Omega\tau}$. The AFT technique is then applied to determine the $\widetilde{W}_{(1,n)}$ and $\tilde{Q}_n$. By a substitution of time history of response in Eq. (23) into nonlinear restoring force expression in Eq. (12) or Eq. (22) for the system under force or displacement excitation, respectively, the time history of the dynamic force $F_{\mathrm{NISE\_dynamic}}(\tau)$ is obtained. Then, discrete Fourier transform is taken on the $F_{\mathrm{NISE\_dynamic}}(\tau)$. Hence the nonlinear force expression of $F_{\mathrm{NISE\_dynamic}}$ in frequency domain is derived, and the complex coefficients of $\tilde{Q}_n$ are determined. Subsequently, by a substitution of those Fourier series expression of response and force into Eqs. (11) or (21), and applying HBM for terms with the same order of n, we have

$$(\mathrm{i}(2n\Omega\zeta_1) - (n\Omega)^2)\widetilde{W}_{(1,n)} = \tilde{T}_n - \tilde{Q}_n, \tag{24}$$

where $\tilde{T}_n$ is the corresponding Fourier coefficients of the excitation term, with $\tilde{T}_1 = F_0$ for the forced system and $\tilde{T}_1 = Z + 2\zeta_1 Z' = Z_0 + \mathrm{i}2\zeta_1\Omega Z_0$ for the base-motion excited system. Recalling that $0 \le n \le N$, we can obtain $(2N + 1)$ nonlinear algebraic equations by balancing the complex terms of Eq. (24). By employing the Newton-Raphson method and the pseudo-arclength continuation method for tracing the solution branches [52], the responses of the mass are calculated. The performance indices can be then determined for further assessment.

3.2.1 Performance assessment for force excited system

For assessment of the vibration isolation system under force excitation, both transmissibility and vibrational energy are taken as performance indicators [35]. The force transmissibility is

$$TR_{\mathrm{f}} = \frac{\max(\,|\Re\{F_{\mathrm{tf}}\}|)}{F_0}, \tag{25}$$

where F_{tf} is the transmitted force with $F_{\mathrm{tf}} = F_{\mathrm{dynamic\_NISE}} + X_1 + 2\zeta_1 X_1'$. The $\Re\{\,\}$ represents taking the real part of the variable.

Using the expression of response in Eq. (23), the time-averaged vibrational energy input (TAVEI) $\bar{P}_{\mathrm{in}}$ is defined as

$$\bar{P}_{\mathrm{in}} = \frac{1}{\tau_2}\Re\int_{\tau_1}^{\tau_1+\tau_2} \Re\{X_1'\}\{F_0\mathrm{e}^{\mathrm{i}\Omega\tau}\}\,\mathrm{d}\tau = \frac{\Re\{(\mathrm{i}\Omega\widetilde{W}_{(1,1)})^*\}F_0}{2}, \tag{26}$$

where $[\tau_1, \tau_1 + \tau_2]$ are time range of taking the average in steady state which can be set as $\tau_2 = 2\pi/\Omega$. ()* marks operation of taking complex conjugate.

The kinetic energy K_{inetic} is also used for the isolation assessment, expressed as

$$K_{\mathrm{inetic}} = \frac{\max(X_1'^2)}{2}. \tag{27}$$

Figures 5-7 depict performance indices under the changes of four design parameters of NISE, including the spring stiffness ratio λ_{k}, the inertance-to-mass ratio λ_{b}, the original spring length L_{s} and the equilibrium height H_1 of NISE. Ω is the non-dimensional frequency in x-axis. The system parameters are fixed at $F_0 = 0.002$ and ζ_1 =0.01. For the investigation of stiffness ratio, the value of λ_k is selected as 0, 2, 3 and 4 while $\lambda_b = 5$, $L_s = 0.7$ and $H_1 = 0.4$. It is noted that the case with $\lambda_k = 0$ represents that only the inerter is embedded in the linkage mechanism of the nonlinear isolator. When examining inertance-to-mass ratio, the value of λ_b is selected as 0, 5 10 and 20 while $\lambda_k = 2$, $L_s = 0.5$ and $H_1 = 0.4$. The case with $\lambda_b = 0$ denotes that only the spring is used in the linkage mechanism of the nonlinear isolator. For the original spring length, the value of L_s is changing between 0.5, 0.55, 0.7 and 0.85 while $\lambda_k = 2$, $\lambda_b = 10$ and $H_1 = 0.4$. In the study of equilibrium height of NISE, the value of H_1 is selected as 0.3, 0.4, 0.5 and 0.6, while $\lambda_k = 2$, $\lambda_b = 5$ and L_s =0.5. Moreover, the result of a linear isolation system without using NISE is also presented for comparison.

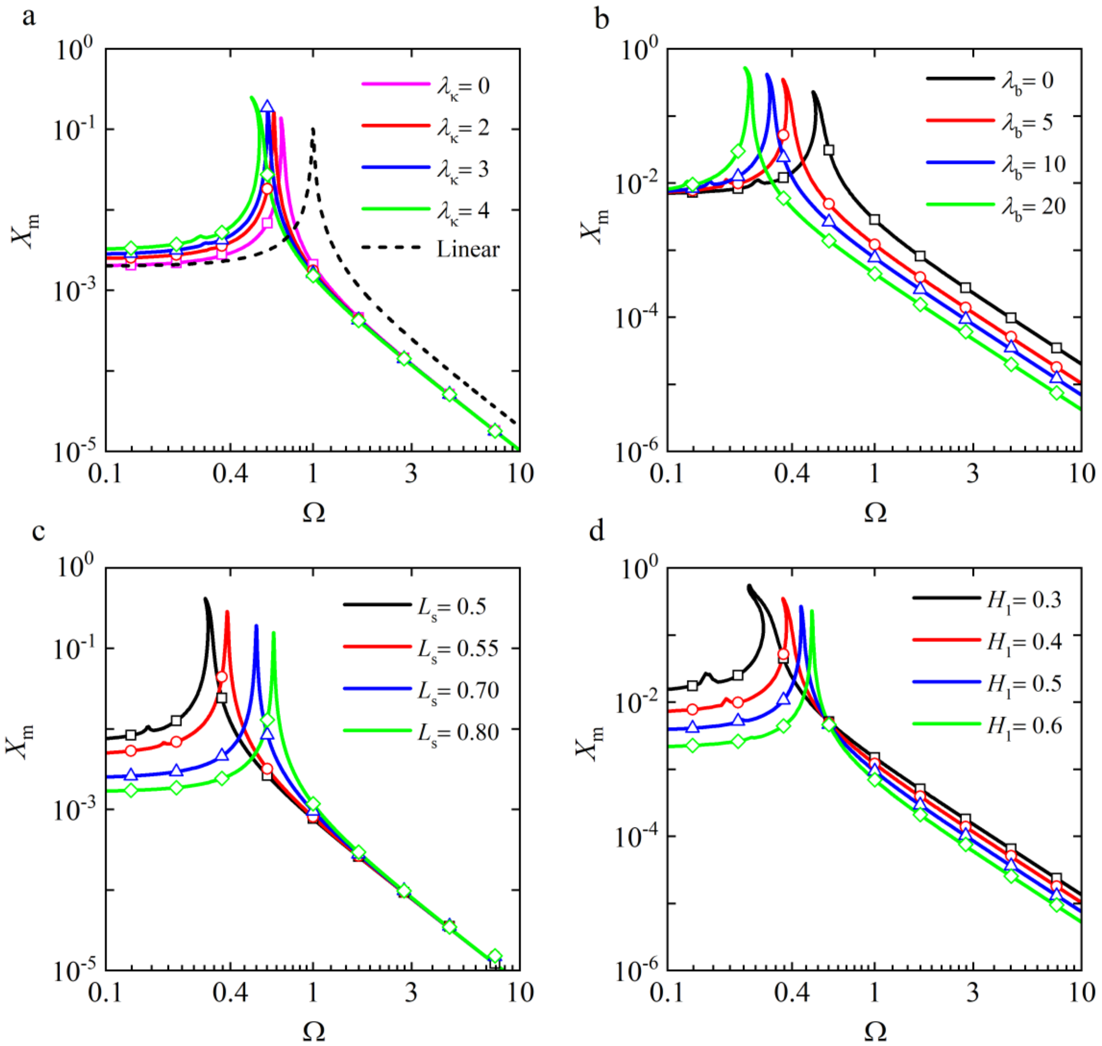

Fig. 5 Maximum displacement response X_m of the equipment under the effect of (a) stiffness ratio of the horizontal spring λ_k , (b) inertance-to-mass ratio λ_b, (c) original spring length L_s and (d) height H_1 of NISE at static equilibrium. Lines: HBM-AFT results, Symbols: RKM results

The variation of maximum displacement X_m under four design parameters of NISE is shown in Fig. 5. From Fig. 5(a), compared to linear case marked by the black dashed line, the use of NISE can shift the resonant peak of the vibration isolation system towards low frequencies, providing a good low-frequency isolation ability. According to the linearized natural frequency and stiffness analysis in subsection 3.1.1, the horizontal spring can result in a negative stiffness, which can lead to a reduced dynamic stiffness and resonant frequency. Moreover, the add-on of the inerter can also decrease the resonant frequency. By comparison to case of $\lambda_{\mathrm{k}} = 0$ with inerter only in NISE, the increase of λ_{k} can further decrease the resonant frequency. A stronger softening behaviour is observed. This is caused by the stronger negative stiffness provided by the NISE with an increasing value of λ_{k}. Fig. 5(b) shows that as inertance λ_{b} of NISE increases, the whole response curve is moved towards left with a higher peak. Fig. 5(c) and 5(d) shows that original spring length L_{s} and equilibrium height H_1 of NISE can significantly affect the system response. A smaller value of L_{s} or H_1 can reduce the corresponding frequency of the peak, while the peak value is increased. The reason is that the nonlinear spring force of NISE depends on L_{s} and H_1 according to Eq. (13), smaller values of two parameters can introduce a smaller dynamic stiffness. Nonlinear inertial force is also related to H_1 due to the geometric nonlinearity of the linkage mechanism. In the low-frequency range, a local maximum value is found when L_{s} and H_1 are small. The system response becomes larger with a smaller value of H_1 in high frequencies, while the changes of L_{s} have minor influence on the response curve.

Figure 6 depicts the force transmissibility TR_{f} under variations of four design parameters of NISE. In Fig. 6(a), by a comparison between the linear isolator and case of $\lambda_{\mathrm{k}} = 0$ using inerter only in NISE, it can be found that the use of inerter can generate an anti-peak in the transmissibility curve. A larger stiffness ratio λ_{k} of the horizontal spring in NISE can not only move the resonant peak towards left but also lower the peak height of TR_{f}. Moreover, the peak is extended to the left, demonstrating a desirable vibration isolation performance. Fig. 6(b) shows that when the inertance value λ_{b} is not zero, the transmissibility values become nearly constant at high frequencies. When λ_{b} increases, frequency of the peak in TR_{f} curve is decreased, while the peak value is decreased first and then increased. Fig. 6(c) shows that a smaller L_{s} can shift the peaks towards left with smaller peak values. Fig. 6(a-c) demonstrates that the anti-peak frequency can be modified by adjusting the parameters of NISE. If the anti-peak frequency is designed to be coincidental with the dominant frequency line spectrum of the installed equipment. Ultra-low force transmission to the ground can be obtained and the vibration transmission is minimized. Fig. 6(d) shows that a reduction of H_1 can twist the peak towards low frequencies and lower its height. The transmissibility value is also decreased at high frequencies but the anti-resonant peak shows little variance. It can be found from Fig. 6 that by tuning the parameters of NISE, the low-frequency force transmission to the ground can be reduced.

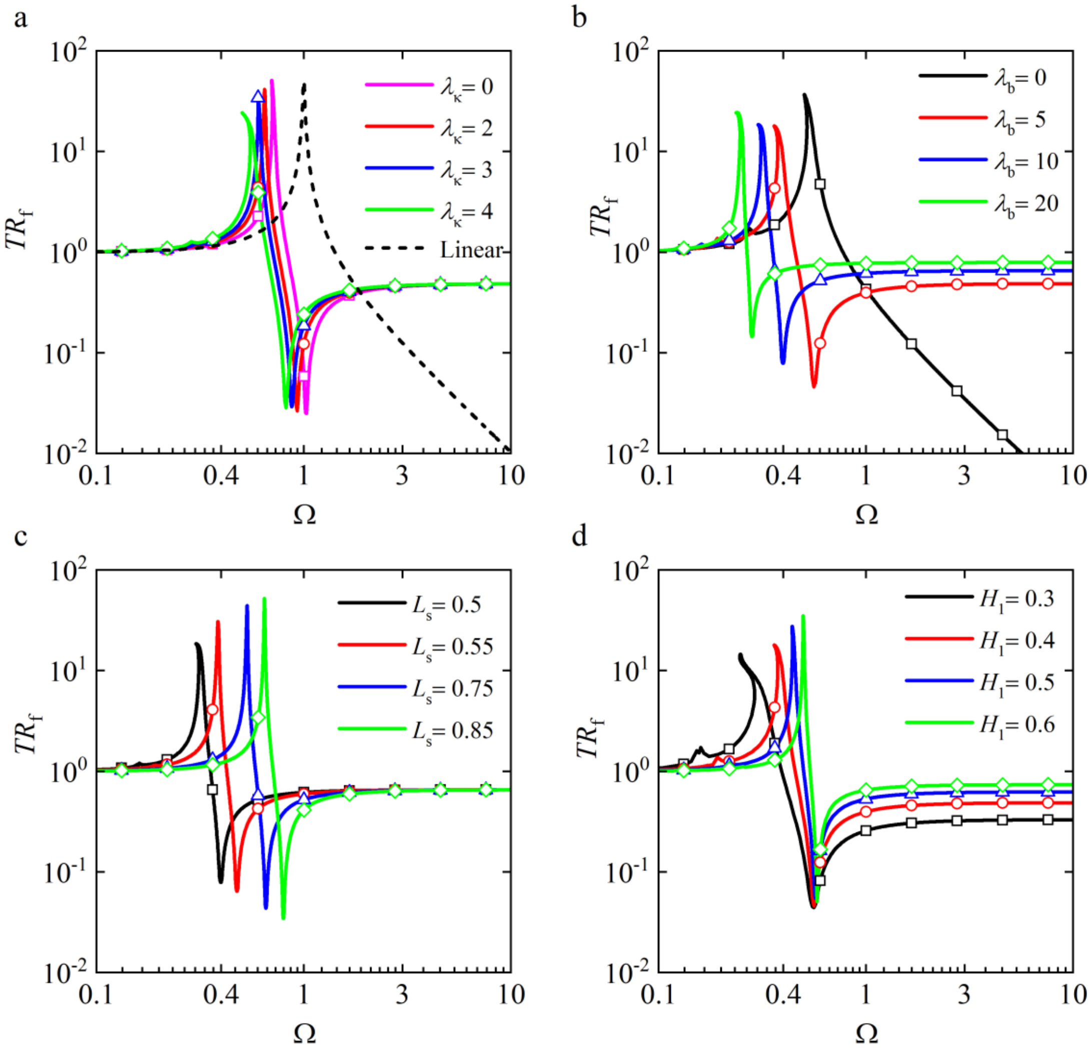

Fig. 6 Force transmissibility under the effect of (a) stiffness ratio of the horizontal spring λ_k, (b) inertance-to-mass ratio λ_b, (c) original spring length L_s and (d) height H_1 of NISE at static equilibrium. Lines: HBM-AFT results, Symbols: RKM results

Figure 7 depicts the time-averaged vibrational energy input TAVEI and kinetic energy. Fig. 7(a) shows compared to the linear isolator, the use of NISE with inerter only (case of $\lambda_k = 0$) can reduce the resonant frequency of TAVEI. With the variations of λ_k, the amount of input energy remains almost unchanged in the area of resonance and high frequencies. Fig. 7(b) shows that increasing the value of λ_b can move the TAVEI curve to the left. The peak value shows minor differences but the values at high frequencies are decreased. Fig. 7(c) and (d) shows that a smaller original spring length L_s or equilibrium height H_1 of NISE can result in a reduced resonant frequency of kinetic energy. In the contrast, peak values of K_{inetic} show little changes. Local peaks can be observed near $\Omega = 0.2$ when the values of L_s and H_1 are small. At high frequencies, the kinetic energy decreases with a larger H_1. Fig. 7 indicates that the peak frequency of vibrational energy input and maximum kinetic energy can be adjusted by NISE. Combining the results in Fig. 6 and 7, it can be summarized that for the SDOF vibration system under force excitation, by selecting a proper value of design parameters of NISE, the low-frequency vibration transmitted to the ground can be considerably controlled.

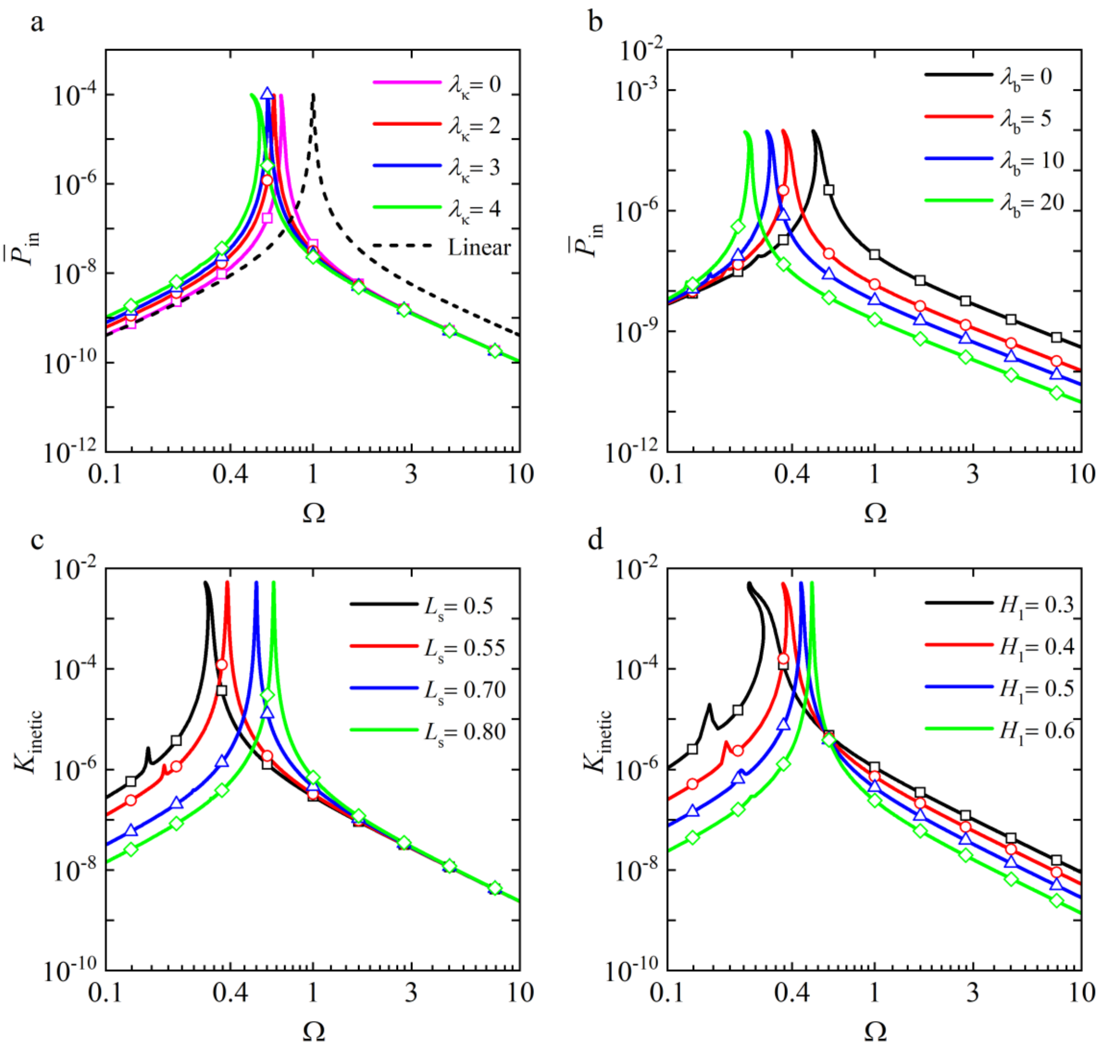

Fig. 7 Time-averaged vibrational energy input under the effect of (a) stiffness ratio of the horizontal spring λ_k , (b) inertance-to-mass ratio λ_b; Kinetic energy of the equipment mass under the effect of (c) original spring length L_s and (d) height H_1 of NISE at static equilibrium. Lines: HBM-AFT results, Symbols: RKM results

3.2.2 Performance assessment for base-motion excited system

For base-motion excited system, the displacement transmissibility TR_{disp} is usually used, which can be defined as

$$TR_{\text{disp}} = \frac{|\Re\{X_{\text{a}}\}|}{Z_0}. \tag{28}$$

where X_{a} denotes the displacement amplitude.

The definition of the kinetic energy is still the same to Eq. (27) in previous section. Based on the law of conservation of energy, the input energy TAVEI for a cycle of excitation is expressed as

$$\bar{P}_{\text{in}} = \frac{1}{\tau_2}\int_{\tau_1}^{\tau_1+\tau_2} 2\zeta_1 (\Re\{Z' - X_1'\})^2 \, \mathrm{d}\tau. \tag{29}$$

Figures 8-10 show the performance of the nonlinear isolator using indices of response, displacement transmissibility and vibrational energy. The parameters are $Z_0 = 0.006$ and $\zeta_1 = 0.01$. Four parameters of NISE are evaluated including 1) the stiffness ratio λ_k with $\lambda_k = 0$, 4, 6 and 8 while

$\lambda_\mathrm{b} = 5$, $L_\mathrm{s} = 0.7$ and $H_1 = 0.4$; 2) the inertance λ_b with λ_b= 0, 5 10 and 20 while $\lambda_\mathrm{k} = 2$, $L_\mathrm{s} = 0.5$ and $H_1 = 0.4$; 3) the original spring length L_s with L_s = 0.5, 0.55, 0.7 and 0.85 while $\lambda_\mathrm{k} = 2$, $\lambda_\mathrm{b} = 10$ and $H_1 = 0.4$; 4) the equilibrium height H_1 of NISE with H_1= 0.3, 0.4, 0.5 and 0.6 while $\lambda_\mathrm{k} = 2$, $\lambda_\mathrm{b} = 10$ and L_s =0.5. The results of a linear isolator system without NISE are also shown as a reference case.

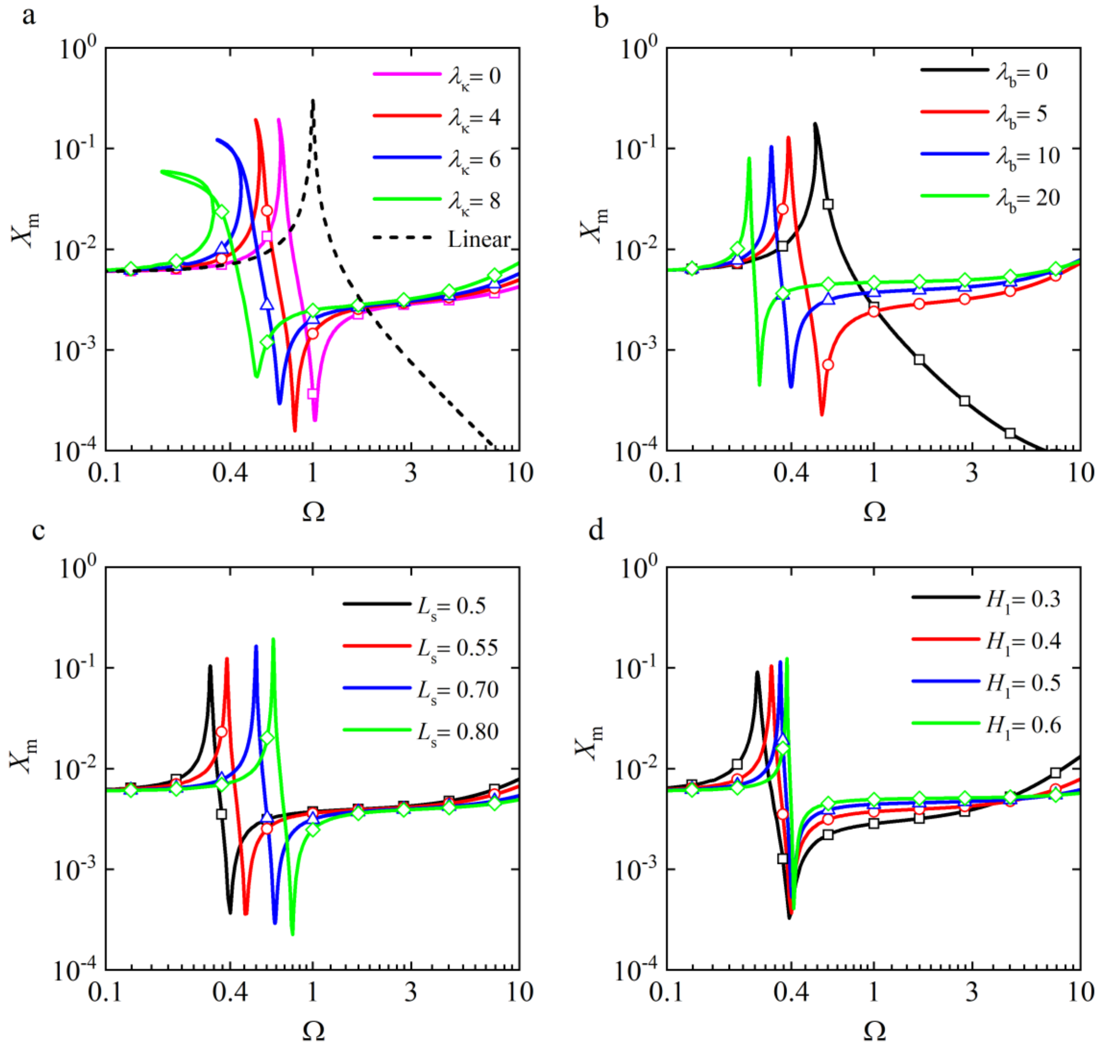

Fig. 8 Maximum displacement response X_m of the equipment under the effect of (a) stiffness ratio of the horizontal spring λ_k , (b) inertance-to-mass ratio λ_b, (c) original spring length L_s and (d) height H_1 of NISE at static equilibrium. Lines: HBM-AFT results, Symbols: RKM results

Figure 8 depicts the variations of the maximum displacement. From Fig. 8(a), by comparing to the case of linear system without NISE, the maximum response displacement in the case of $\lambda_\mathrm{k} = 0$ with inerter only in the NISE is decreased and resonant frequency is reduced. Anti-resonance is observed due to the usage of inerter. With addition of spring in NISE ($\lambda_\mathrm{k} \neq 0$), the response peak and anti-peak are lowered, and the peak is extended more towards low frequencies. However, the dynamic response is increased at high frequencies with the inclusion of NISE. It shows NISE is better to be used in isolating low-frequency vibration from foundation. Fig. 8(b) shows the combination of inerter and spring in NISE ($\lambda_\mathrm{b} \neq 0$) can lower the peak of X_m. The peak and anti-peak frequencies can be altered by modifying the inertance λ_b. Fig. 8(c) and (d) shows a decrease of original spring length L_s or equilibrium height H_1 of NISE can cause reduction in resonant frequency and peak height of displacement response. It is also found that the anti-peak is insensitive to the equilibrium height H_1 of NISE.

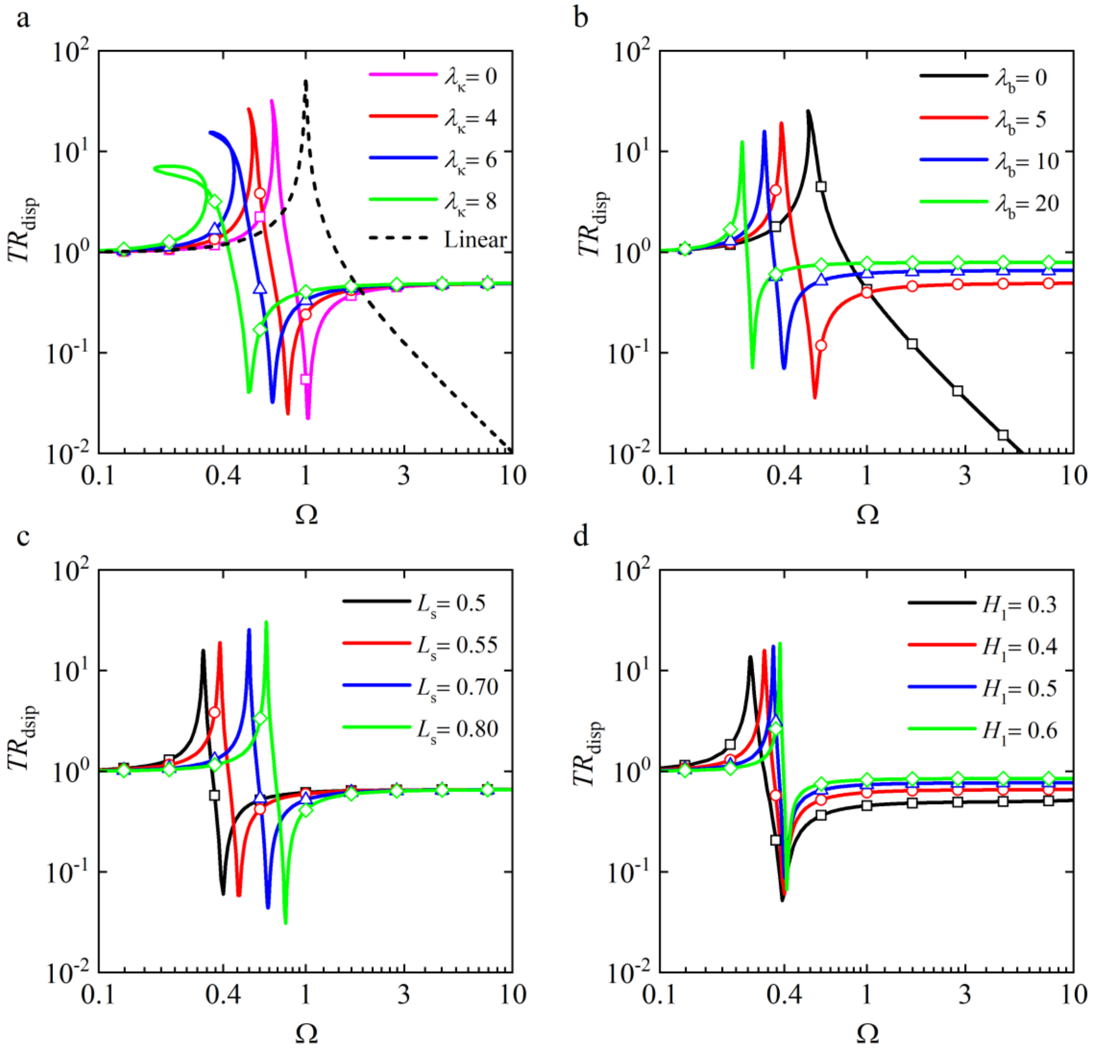

Fig. 9 Displacement transmissibility TR_{disp} to the equipment under the effect of (a) stiffness ratio of the horizontal spring λ_{k}, (b) inertance-to-mass ratio λ_{b}, (c) original spring length L_{s} and (d) height H_1 of NISE at static equilibrium. Lines: HBM-AFT results, Symbols: RKM results

Figure 9 shows the displacement transmissibility under influence of design parameters of NISE. In Fig. 9(a), compared to the reference linear system case, the nonlinear isolator case $\lambda_{\mathrm{k}} = 0$ with inerter only in NISE can lower the level of TR_{disp} at peak frequency and provide an ultra-low TR_{disp} in the original resonance frequency for the linear system. Moreover, according to the linearized stiffness analysis in the previous section, a larger value of λ_{k} can lead to a smaller dynamic stiffness. Therefore, as shown in Fig. 9(a), peak and anti-peak frequencies of TR_{disp} are changed with the value of stiffness ratio λ_{k}. In addition, the TR_{disp} curve is twisted towards low frequencies when using a larger λ_{k}. Fig. 9(b) shows both inerter and spring in NISE can benefit the isolation of low-frequency vibration. The peak and anti-peak frequencies are reduced when using a larger inertance value λ_{b}. In the contrast, the TR_{disp} at high frequencies is increased with λ_{b}. Fig. 9(c) shows that a smaller value of L_{s} can move the

TR_{disp} curve to the left and the peaks values are reduced. At high frequencies, the values of TR_{disp} show little difference in the changing value of L_{s}. Fig. 9(d) shows that reducing the equilibrium height H_1 can bend the TR_{disp} peak to the low frequencies and reduce the TR_{disp} at high frequencies. From Fig. 9, it is demonstrated that increasing the λ_{k} and λ_{b}, or reducing the L_{s} and H_1 can attenuate low-frequency vibration. The frequency band of ultra-low TR_{disp} is obtained by using NISE and it can be adjusted by designing those parameters of NISE.

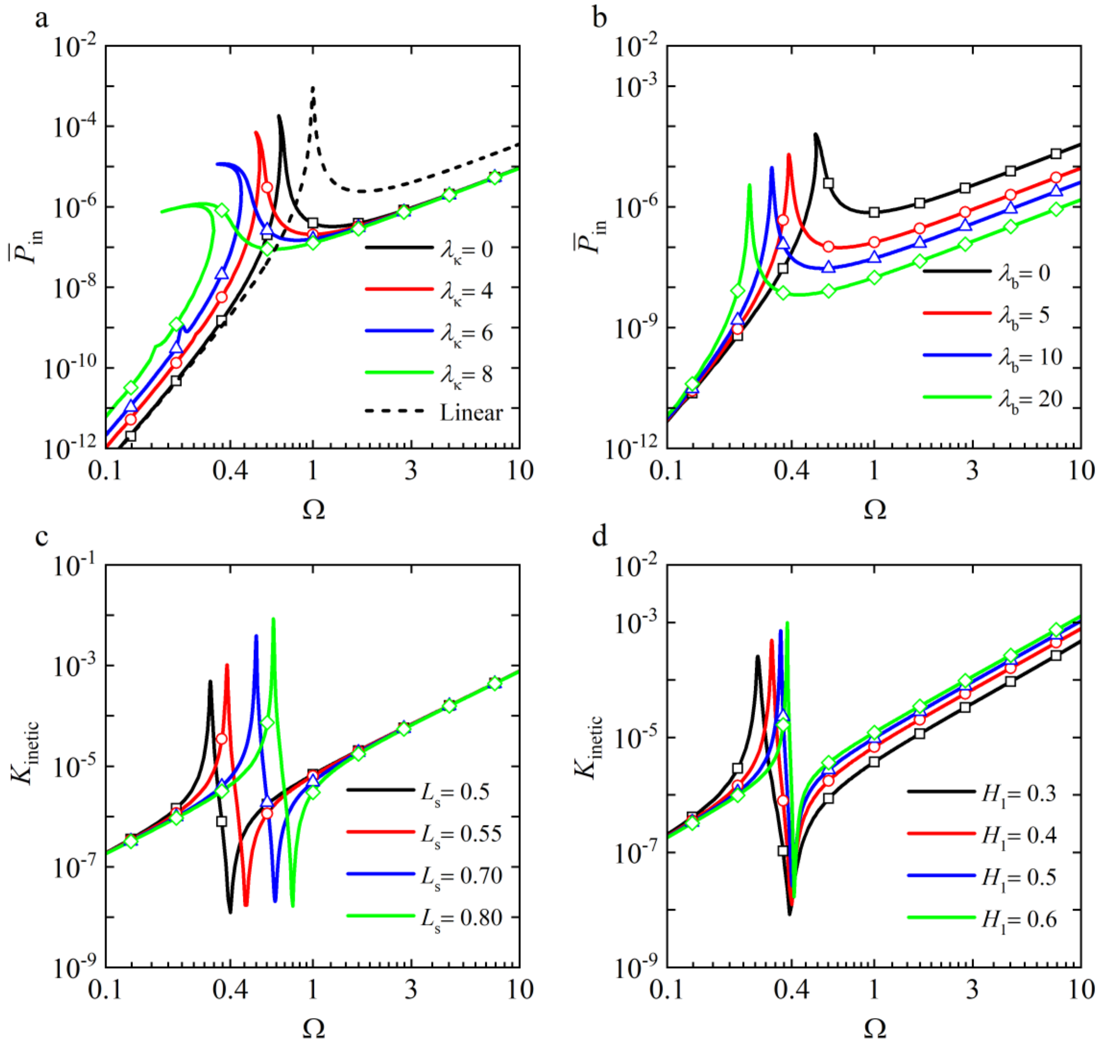

Fig. 10 Time-averaged vibrational energy input TAVEI under the effect of (a) stiffness ratio of the horizontal spring λ_{k} , (b) inertance-to-mass ratio λ_{b}; Kinetic energy of the equipment mass under effect of (c) original spring length L_{s} and (d) height H_1 of NISE at static equilibrium. Lines: HBM-AFT results, Symbols: RKM results

Figure 10 depicts the variations of TAVEI and K_{inetic}. Fig. 10(a) shows that the NISE can reduce the amount of vibrational input energy. Increasing λ_{k} can further lower the peak of $\bar{P}_{\mathrm{in}}$ and twist the peak to the left. Fig. 10(b) demonstrates that increasing the inertance λ_{b} can lower the peak and reduce the resonant frequency. From Fig. 10(a) and (b), it is found that the TAVEI is sensitive to the variation of inertance at high frequencies and sensitive to the changes in λ_{k} at low frequencies. This phenomenon demonstrates that the spring and inerter in NISE have different impacts on the vibrational energy. Fig 10(c) and (d) shows with decreasing original spring length L_{s} and equilibrium height H_1 of NISE, the kinetic energy K_{inetic} is reduced. An anti-resonance is observed in kinetic energy curve, indicating that vibrational energy transfer to the mass can be suppressed considerably in the certain frequency band. At high frequencies, K_{inetic} is also lowered with a decreasing value of H_1. Fig. 10 demonstrates the benefits of using NISE in the system subjected to foundation excitation. The vibrational energy input and transmitted to the mass can be reduced.

4. NISE vibration isolator in 2DOF system

4.1 Modelling of 2DOF isolation system

Considering the need for vibration isolation of mechanical systems in vessels or aircraft whose mounting bases are not rigid, the characteristic of the proposed NISE applied in a 2DOF system with flexible base structure is investigated. As shown in Fig. 11, equipment mass m_1 is installed on the flexible base m_{fb} via the NISE-based vibration isolator. A harmonic force is applied on mass m_1 for the simulation of excitation by the operation of the equipment. The stiffness and damping of the flexible base are k_{fb} and c_{fb}. After the installation of the equipment mass, the system reaches equilibrium and terminal distance AB becomes $h = h_1$. The response displacement of the equipment and the base are x_1 and x_{fb}, respectively. The reference point of $x_1 = x_{\text{fb}} = 0$ is set when the system is at static equilibrium with $h = h_1$.

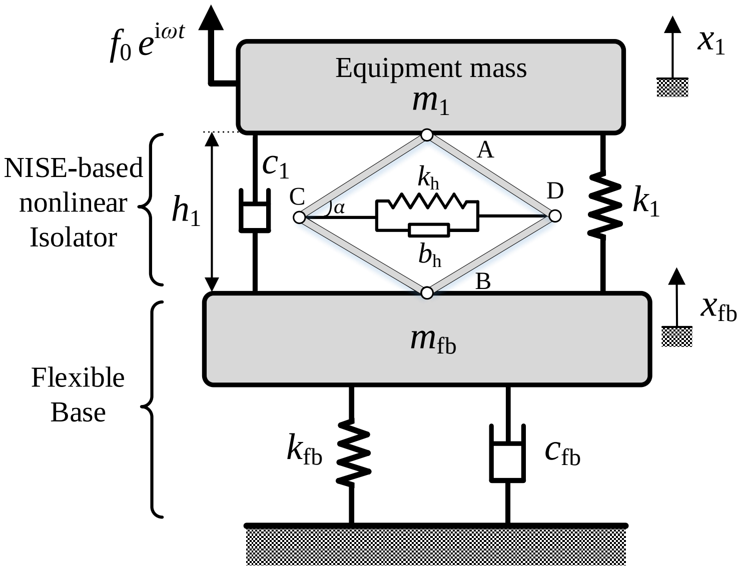

Fig. 11 Model of 2DOF NISE-based vibration isolation system with a flexible base

The equation motion of the system is:

$$\begin{bmatrix} m_1 & 0 \\ 0 & m_{\text{fb}} \end{bmatrix} \begin{Bmatrix} \ddot{x}_1 \\ \ddot{x}_{\text{fb}} \end{Bmatrix} + \begin{bmatrix} k_1 & -k_1 \\ -k_1 & k_1 + k_{\text{fb}} \end{bmatrix} \begin{Bmatrix} x_1 \\ x_{\text{fb}} \end{Bmatrix} + \begin{bmatrix} c_1 & -c_1 \\ -c_1 & c_{\text{fb}} + c_1 \end{bmatrix} \begin{Bmatrix} \dot{x}_1 \\ \dot{x}_{\text{fb}} \end{Bmatrix} + \begin{Bmatrix} f_{\text{NISE}}(h, \dot{h}, \ddot{h}) + m_1 g \\ -f_{\text{NISE}}(h, \dot{h}, \ddot{h}) - m_1 g \end{Bmatrix} = \begin{Bmatrix} f_0 e^{i\omega t} \\ 0 \end{Bmatrix}, \quad (30)$$

where

$$f_{\mathrm{NISE}}\left(h,\dot{h},\ddot{h}\right)=k_{\mathrm{h}}(h_1+x_1-x_{\mathrm{fb}})\left(\frac{l_{\mathrm{s}}}{\sqrt{4l_{\mathrm{rod}}^2-(h_1+x_1-x_{\mathrm{fb}})^2}}-1\right)+b_{\mathrm{h}}\left(\frac{(h_1+x_1-x_{\mathrm{fb}})^2(\ddot{x}_1-\ddot{x}_{\mathrm{fb}})}{4l_{\mathrm{rod}}^2-(h_1+x_1-x_{\mathrm{fb}})^2}+\frac{4l_{\mathrm{rod}}^2(h_1+x_1-x_{\mathrm{fb}})(\dot{x}_1-\dot{x}_{\mathrm{fb}})^2}{\left(4l_{\mathrm{rod}}^2-(h_1+x_1-x_{\mathrm{fb}})^2\right)^2}\right), \quad (31)$$

By introducing the following parameters

$$X_{\mathrm{fb}}=\frac{x_{\mathrm{fb}}}{2l_{\mathrm{rod}}},\quad \omega_{\mathrm{fb}}=\sqrt{\frac{k_{\mathrm{fb}}}{m_{\mathrm{fb}}}},\quad \nu_{\mathrm{fb}}=\frac{\omega_{\mathrm{fb}}}{\omega_1},\quad \zeta_{\mathrm{fb}}=\frac{c_{\mathrm{fb}}}{2m_{\mathrm{fb}}\omega_{\mathrm{fb}}},\quad \beta_{\mathrm{fb}}=\frac{m_{\mathrm{fb}}}{m_1}, \quad (32)$$

where X_{fb} is the base displacement, ω_{fb} and ν_{fb} denote the resonant frequency and frequency ratio of flexible base, respectively. ζ_{fb} and β_{fb} are the damping and mass ratios of the base. Then Eq. (30) is transformed using Eq. (32), expressed as

$$\begin{bmatrix}1 & 0\\ 0 & \beta_{\mathrm{fb}}\end{bmatrix}\begin{Bmatrix}X_1''\\ X_{\mathrm{fb}}''\end{Bmatrix}+\begin{bmatrix}2\zeta_1 & -2\zeta_1\\ -2\zeta_1 & 2(\zeta_1+\zeta_{\mathrm{fb}}\beta_{\mathrm{fb}}\nu_{\mathrm{fb}})\end{bmatrix}\begin{Bmatrix}X_1'\\ X_{\mathrm{fb}}'\end{Bmatrix}+\begin{bmatrix}1 & -1\\ -1 & 1+\beta_{\mathrm{fb}}{\nu_{\mathrm{fb}}}^2\end{bmatrix}\begin{Bmatrix}X_1\\ X_{\mathrm{b}}\end{Bmatrix}+\begin{Bmatrix}F_{\mathrm{NISE}}(H,H',H'')+\frac{m_1g}{2l_{\mathrm{rod}}k_1}\\ -F_{\mathrm{NISE}}(H,H',H'')-\frac{m_1g}{2l_{\mathrm{rod}}k_1}\end{Bmatrix}=\begin{Bmatrix}F_0\mathrm{e}^{\mathrm{i}\Omega\tau}\\ 0\end{Bmatrix}, \quad (33)$$

where

$$F_{\mathrm{NISE}}(H,H',H'')=\lambda_{\mathrm{k}}(X_1-X_{\mathrm{fb}}+H_1)\left(\frac{L_{\mathrm{s}}}{\sqrt{1-(X_1-X_{\mathrm{fb}}+H_1)^2}}-1\right)+\lambda_{\mathrm{b}}\left(\frac{\left(X_1'-X_{\mathrm{fb}}'\right)^2(X_1-X_{\mathrm{fb}}+H_1)^2}{1-(X_1-X_{\mathrm{fb}}+H_1)^2}+\frac{(X_1''-X_{\mathrm{fb}}'')(X_1-X_{\mathrm{fb}}+H_1)}{(1-(X_1-X_{\mathrm{fb}}+H_1)^2)^2}\right). \quad (34)$$

It is noted that the equipment load is balanced by NISE and linear vertical spring at the equilibrium position of $h=h_1$.

To solve the governing equation, the HBM-AFT is applied. The Eq. (23) is reused for approximation of response of equipment mass and dynamic force of NISE. The displacement response of the base m_{fb} is estimated by $X_{\mathrm{fb}}=\sum_{n=0}^{N}\widetilde{W}_{(\mathrm{fb},n)}\,\mathrm{e}^{in\Omega\tau}$. By a substitution of responses approximation into Eq. (23) with $F_{\mathrm{NISE}}(H,H',H'')$ defined by Eq. (34), the time history of dynamic force $F_{\mathrm{NISE\_dynamic}}(\tau)$ of NISE is obtained. The coefficient $\tilde{Q}_n$ can then be determined by taking Fourier transform on the $F_{\mathrm{NISE\_dynamic}}(\tau)$. By applying the HBM on Eq. (33), the n-th order terms of Eq. (33) are balanced and expressed as

$$\left(-(n\Omega)^2\begin{bmatrix}1 & 0\\ 0 & \beta_{\mathrm{fb}}\end{bmatrix}+\mathrm{i}(n\Omega)\begin{bmatrix}2\zeta_1 & -2\zeta_1\\ -2\zeta_1 & 2(\zeta_1+\zeta_{\mathrm{fb}}\beta_{\mathrm{fb}}\nu_{\mathrm{fb}})\end{bmatrix}+\begin{bmatrix}1 & -1\\ -1 & 1+\beta_{\mathrm{fb}}\nu_{\mathrm{fb}}^2\end{bmatrix}\right)\begin{Bmatrix}\widetilde{W}_{(1,n)}\\ \widetilde{W}_{(\mathrm{fb},n)}\end{Bmatrix}=\begin{Bmatrix}F_0\\ 0\end{Bmatrix}+\begin{Bmatrix}-\tilde{Q}_n\\ \tilde{Q}_n\end{Bmatrix}. \quad (35)$$

Due to the degree of freedom of the system being 2 and $0\le n\le N$, there are $2(2N+1)$ algebraic equations in total. The solution can be determined by using the Newton-Raphson method. The pseudo-arclength continuation method is also used in the calculation. The results are compared with those obtained by the RK numerical integration method.

4.2 Assessment of the 2DOF isolation system

The force transmissibility TR_{fb} to the flexible base is

$$TR_{\mathrm{fb}} = \frac{\max(\,|F_{\mathrm{tfb}}|)}{F_0}, \tag{36}$$

where transmitted force is the sum of dynamic force of NISE and spring and the damper force as $F_{\mathrm{tfb}} = F_{\mathrm{NISE\_dynamic}}(H, H', H'') + X_1 - X_{\mathrm{fb}} + 2\zeta_1(X_1' - X_{\mathrm{fb}}')$.

The vibrational energy transfer is usually used for quantification of vibration transmission from one sub-structure to another, here the time-averaged vibrational energy transfer (TAVET) $\bar{P}_{\mathrm{fb}}$ is taken for the indicator of vibration isolation performance, expressed as

$$\bar{P}_{\mathrm{fb}} = \frac{1}{\tau_2}\int_{\tau_1}^{\tau_1+\tau_2} 2\zeta_{\mathrm{fb}}\beta_{\mathrm{fb}}\nu_{\mathrm{fb}}(\Re\{X_{\mathrm{fb}}'\})^2\,\mathrm{d}\tau, \tag{37}$$

where X_{fb}' can be approximated by the Fourier series and Eq. (37) can be transformed as

$$\bar{P}_{\mathrm{fb}} = \frac{1}{2}\Re\left\{\left(\sum_{n=0}^{N} in\Omega\widetilde{W}_{(\mathrm{fb},n)}\right)^{*}\left(2\zeta_{\mathrm{fb}}\beta_{\mathrm{fb}}\nu_{\mathrm{fb}}\sum_{n=0}^{N} in\Omega\widetilde{W}_{(\mathrm{fb},n)}\right)\right\} = \zeta_{\mathrm{fb}}\beta_{\mathrm{fb}}\nu_{\mathrm{fb}}\left|\sum_{n=0}^{N} in\Omega\widetilde{W}_{(\mathrm{fb},n)}\right|^{2}. \tag{38}$$

By using the definition of TAVEI in subsection 3.2.1, the power transmission ratio is obtained

$$R_{\mathrm{fb}} = \frac{\bar{P}_{\mathrm{fb}}}{\bar{P}_{\mathrm{in}}} = \frac{2\zeta_{\mathrm{fb}}\beta_{\mathrm{fb}}\nu_{\mathrm{fb}}\left|\sum_{n=0}^{N} in\Omega\widetilde{W}_{(\mathrm{fb},n)}\right|^{2}}{F_0\Re\left\{\left(\mathrm{i}\Omega\widetilde{W}_{(1,1)}\right)^{*}\right\}}. \tag{39}$$

Figures 12-14 present the influence of four parameters of NISE on 2DOF system with flexible base structure. The parameters of system are $\beta_{\mathrm{fb}} = \nu_{\mathrm{fb}} = 1$, $F_0 = 0.0015$, $\zeta_1 = \zeta_{\mathrm{fb}}$ =0.01. In the evaluation of stiffness ratio, the value of λ_{k} is changing between 0, 3, 4 and 5 while $\lambda_{\mathrm{b}} = 5$, $L_{\mathrm{s}} = 0.7$ and $H_1 = 0.4$. When investigating inertance λ_{b}, the value is chosen as 0, 5 10 and 20 while $\lambda_{\mathrm{k}} = 2$, $L_{\mathrm{s}} = 0.5$ and $H_1 = 0.4$. For the investigation on the original spring length L_{s}, its value is varying between 0.5, 0.55, 0.7 and 0.85 while $\lambda_{\mathrm{k}} = 2$, $\lambda_{\mathrm{b}} = 10$ and $H_1 = 0.4$. As for the equilibrium height H_1 of NISE, the value is selected as 0.3, 0.4, 0.5 and 0.6, while $\lambda_{\mathrm{k}} = 2$, $\lambda_{\mathrm{b}} = 5$ and L_{s} =0.5. For comparison, the linear system case without NISE is also shown.

Figure 12 depicts the force transmission to the base under four design parameter sets of the NISE. Fig. 12(a) shows compared to the linear reference case, the addition of NISE can lower remarkably the second peak height of TR_{fb} near $\Omega = 0.9$. By adjusting the value of λ_{k} in NISE, the second peak in the original linear system can be minimized, demonstrating enhanced vibration mitigation. By increasing the value of λ_{k}, the first peak near $\Omega = 0.4$ is lowered and twisted to the left. Fig. 12(b) shows that peak and anti-peak frequencies of TR_{fb} can be tailored by designing the value of inertance ratio λ_{b}. The frequency range of $TR_{\mathrm{fb}} < 1$ at low frequencies can be widened by increasing λ_{b}. As a result, the system can provide a superior ultra-low force transmission. Fig. 12(c) and (d) shows reducing original spring length L_{s} and equilibrium height H_1 of NISE can lower the first peak of TR_{fb} but increase the second. Meanwhile, the resonant frequencies of two peaks in TR_{fb} curve are both reduced and the frequency range of $TR_{\mathrm{fb}} < 1$ becomes broader. It is shown that the values of TR_{fb} are reduced at high frequencies as H_1 decreases. From Fig. 12(b-d), it can be found that the frequency bandwidth and range for ultra-low values of TR_{fb} (i.e., the frequency band of $TR_{\mathrm{fb}} < 1$ at low frequencies) can be designed by changing the values of λ_b, L_s and H_1. The low-frequency vibration force transmission from the equipment to the base can then be significantly suppressed.

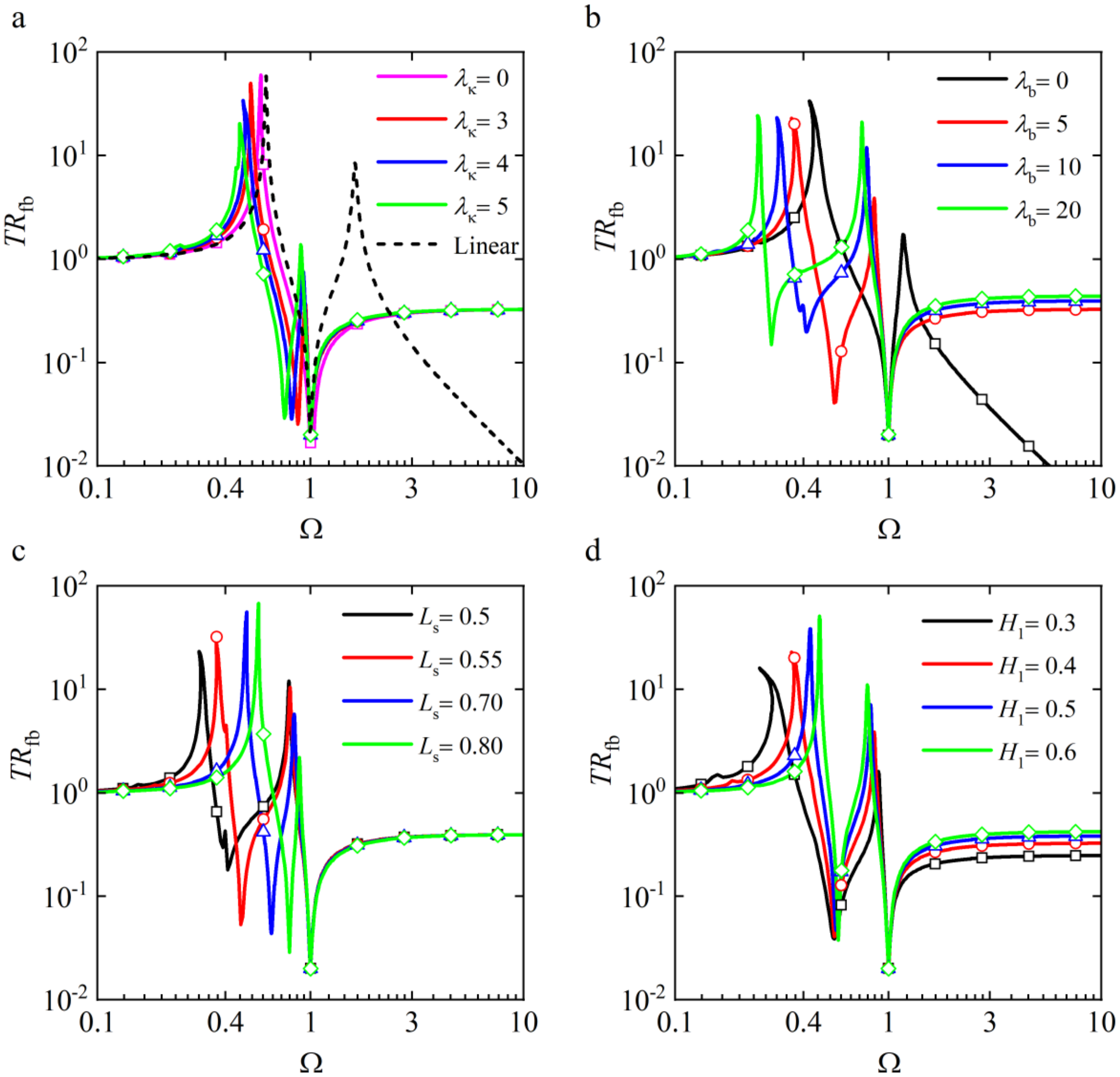

Fig. 12 Force transmissibility TR_{fb} to the base under the effect of (a) stiffness ratio of the horizontal spring λ_k, (b) inertance-to-mass ratio λ_b, (c) original spring length L_s and (d) height H_1 of NISE at static equilibrium. Lines: HBM-AFT results, Symbols: RKM results

Figure 13 shows the variations of TAVET from vibrating equipment to the base through NISE. Fig. 13(a) shows that two peaks of $\bar{P}_{fb}$ are observed in the linear case while an extra anti-peak is noticed in the cases with NISE. It is shown that two positive peaks of $\bar{P}_{fb}$ are lowered when the NISE is added into the isolation system. The heights of the first peak of $\bar{P}_{fb}$ is reduced when using a larger λ_k while the second peak is lowered with a smaller λ_k. Fig. 13(b) shows frequencies of peaks can be moved left by increasing λ_b. The first peak value decreases, which can contribute to low-frequency vibration mitigation. Fig. 13(c) and (d) shows variations in original spring length L_s and equilibrium height H_1 are mainly taking the effect on the first peak and anti-peak of the $\bar{P}_{fb}$ curve. The reduction of L_s can reduce the resonant frequencies of the peaks while the decrease of H_1 will twist the first peak towards low-frequencies. Moreover, a smaller L_s or H_1 can significantly lower the amount of energy transfer at the first peak frequency. Combining Figs. 12 and 13, it demonstrates by inserting NISE into a linear isolator mounted on a flexible base, the vibration transmission at low frequencies to the base can be effectively suppressed.

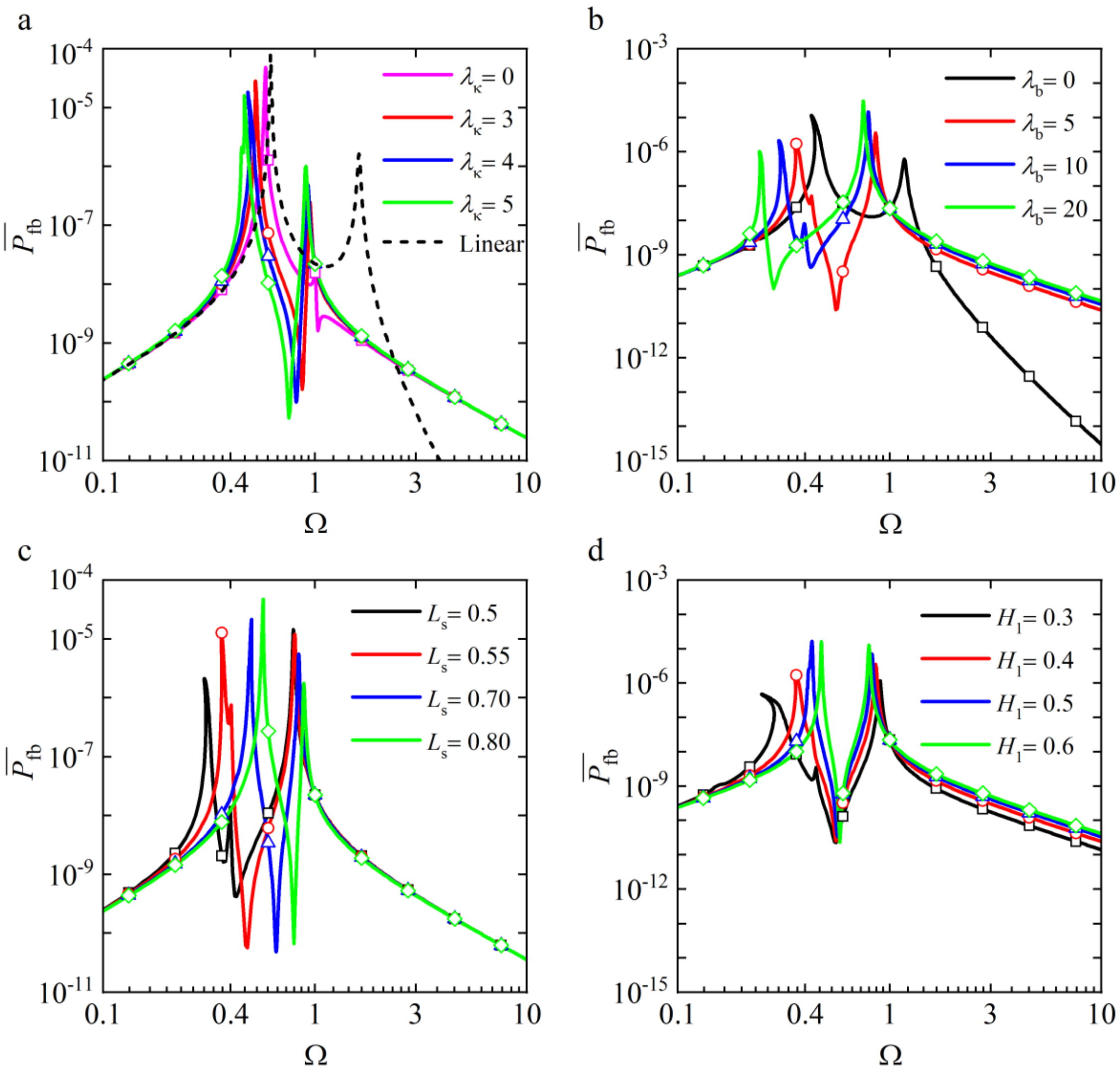

Fig. 13 Time-averaged energy transfer $\bar{P}_{\mathrm{fb}}$ to the base under the effect of (a) stiffness ratio of the horizontal spring λ_{k} , (b) inertance-to-mass ratio λ_{b}, (c) original spring length L_{s} and (d) height H_1 of NISE at static equilibrium. Lines: HBM-AFT results, Symbols: RKM results

Figure 14 shows the variations of energy transfer ratio R_{fb}. Fig. 14(a) shows compared to the linear reference case, the NISE-based isolator can reduce R_{fb} at low frequencies between $\Omega \approx 0.1$ and $\Omega \approx 2$. It is interesting to find an anti-resonance in R_{fb} curve and its frequency as well as its value can be reduced by increasing the value of λ_{k}, which can enhance the isolation performance. In addition, the values of R_{fb} are also reduced at low frequencies with a larger λ_{k}. Fig. 16(b) shows the case of NISE without inerter ($\lambda_{\mathrm{b}} = 0$) cannot generate the anti-peak. When increasing λ_{b} from 0 to 20, the anti-peak is found in the R_{fb} curve and the peak is moved to the low frequencies. Fig. 14(c) and (d) shows reducing original spring length L_{s} and equilibrium height H_1 can lower the ratio of energy transfer in low-frequency range, particularly for $0.1 < \Omega < 0.4$, demonstrating a good performance of NISE. Moreover, a smaller value of H_1 can reduce the R_{fb} in the high-frequency range. Extra peaks can be found in the curve near $\Omega = 0.4$, which are possibly related to the super-harmonic responses of the system. Fig. 14 suggests that the vibration energy transfer can be minimized by tuning the design parameters of NISE.

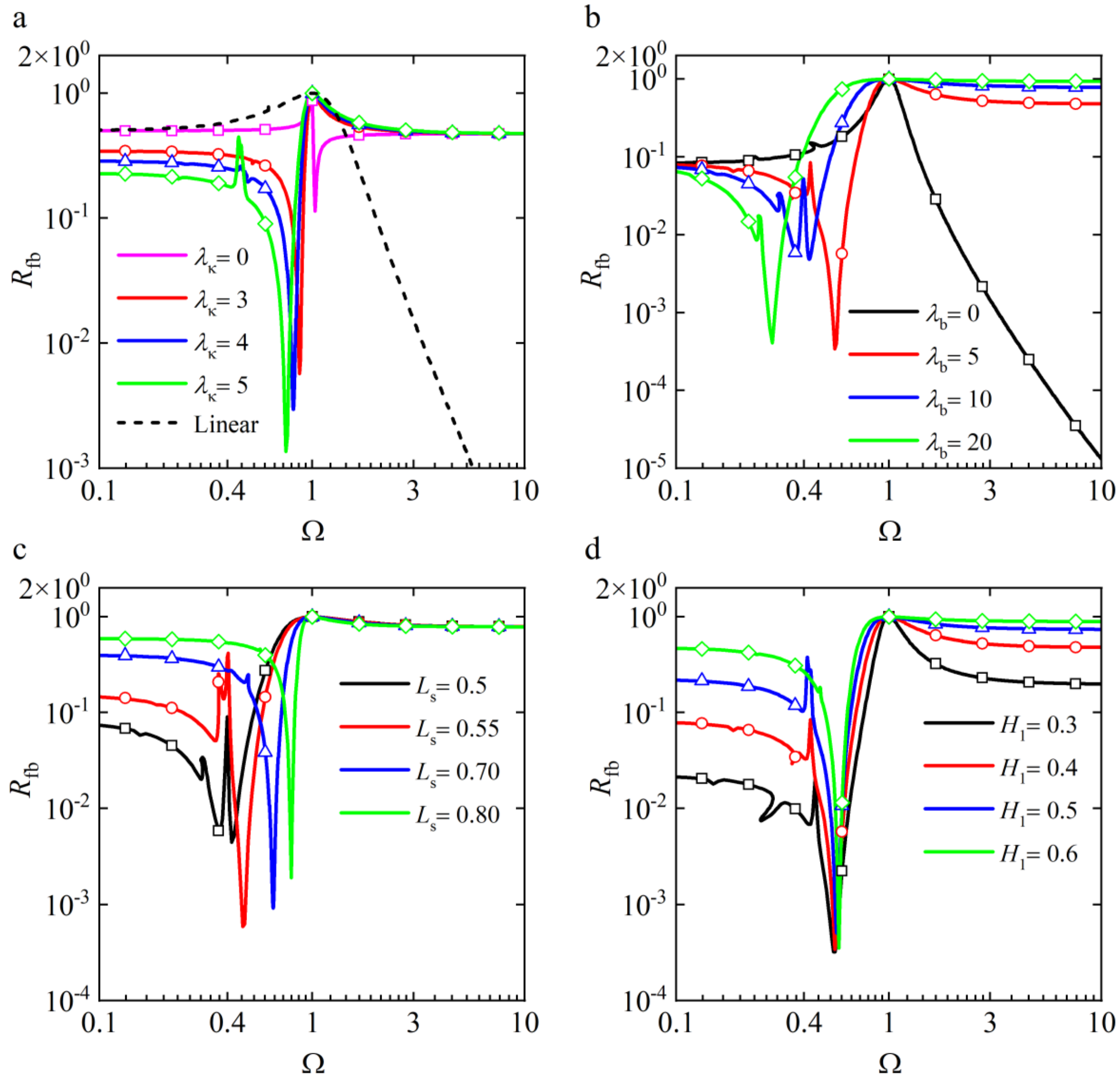

Fig. 14 Ratio of vibration energy transmission R_{fb} to the base under the effect of (a) stiffness ratio of the horizontal spring λ_k, (b) inertance-to-mass ratio λ_b, (c) original spring length L_s and (d) height H_1 of NISE at static equilibrium. Lines: HBM-AFT results, Symbols: RKM results

5. Conclusions

This research proposed a hybrid geometrically nonlinear inertial and stiffness element (NISE) for enhancement of vibration isolation in SDOF system under force and base-motion excitation, and a 2DOF system with a flexible mounting base for simulating the environment of ship and aircraft. The HBM-AFT and RKM were used for the determination of performance indicators of vibration isolator including transmissibility and energy flow indices. The results show that the NISE can improve substantially the effectiveness on isolating low frequency vibration either in SDOF systems or in 2DOF system. The combination of spring and inerter in the linkage mechanism outperforms the one with spring or inerter only in linkage mechanism. The peaks in the curve of displacement response, transmissibility and energy flow indices are suppressed and moved to low frequencies. A frequency band with ultra-low transmissibility, kinetic energy and vibrational energy transfer can be obtained by adding NISE into linear isolator in low frequencies. The frequency band can be tailored by designing the structure parameters of NISE to meet the main excitation frequency of vibration source such as marine main engines and auxiliaries, hence the NISE-based nonlinear isolator can effectively attenuate vibration transmission between the machine~~s~~ and ~~foundation~~mounting base. The low-frequency line-spectrum of dynamic systems such as underwater vehicle can be significantly suppressed.

Declaration of competing interest:

On behalf of all authors, the corresponding author states that there is no conflict of interest.

Acknowledgements

This work has been supported by the National Natural Science Foundation of China under Grant numbers 12202152, 51839005 and 12172185.

Data availability

The data supporting this study's findings are available from the corresponding author, upon reasonable request.

References

[1] Ruan Y, Liang X, Hua X, Zhang C, Xia H, Li C (2021) Isolating low-frequency vibration from power systems on a ship using spiral phononic crystals. Ocean Eng 225: 108804.

[2] Harris CM, Piersol AG (2002) Shock and vibration handbook. McGraw-Hill, New York.

[3] Zhang H, Li P, Jin H, Bi R, Xu D (2022) Nonlinear wave energy dissipator with wave attenuation and energy harvesting at low frequencies. Ocean Eng 266: 112935.

[4] Zhang, Y., Cheng, J., Xu, W., Wang, C., Liu, J., Li, Y., & Yang, S. (2022). Particle damping vibration absorber and its application in underwater ship. J Vib Eng Technol. https://doi.org/10.1007/s42417-022-00700-y

[5] Chen D, Zi H, Li Y, Li X (2021) Low frequency ship vibration isolation using the band gap concept of sandwich plate-type elastic metastructures. Ocean Eng 235: 109460.

[6] Yan B, Ma H, Zhang L, Zheng W, Wang K, Wu C (2020) A bistable vibration isolator with nonlinear electromagnetic shunt damping. Mech Syst Signal Process 136: 106504.

[7] Hao RB, Lu ZQ, Ding H, Chen LQ (2022) Orthogonal six-DOFs vibration isolation with tunable high-static-low-dynamic stiffness: Experiment and analysis. Int J Mech Sci 222: 107237.

[8] Xing X, Chen Z, Feng Z (2022) A variable stiffness and damping control strategy for improving vibration isolation performances in low-frequency excitation. J Vib Eng Technol. https://doi.org/10.1007/s42417-022-00659-w

[9] Fang H, Liu Z, Lei M, Duan L (2022) A high-stiffness sandwich structure with a tristable core for low-frequency vibration isolation. J Vib Eng Technol 10(5): 1989-2003.

[10] Ibrahim RA (2008) Recent advances in nonlinear passive vibration isolators. J Sound Vib 314(3-5): 371–452.

[11] Han WJ, Lu ZQ, Niu MQ, Chen LQ (2022) A high-static-low-dynamics stiffness vibration isolator via an elliptical ring. Mech Syst Signal Process 162: 108061.

[12] Carrella A, Brennan MJ, Waters TP, Lopes Jr. V (2012) Force and displacement transmissibility of a nonlinear isolator with high-static-low-dynamic-stiffness. Int J Mech Sci 55: 22-29.

[13] Yang J, Xiong YP, Xing JT (2013) Dynamics and power flow behaviour of a nonlinear vibration isolation system with a negative stiffness mechanism. J Sound Vib 332: 167-183.

[14] Shaw AD, Neild SA, Wagg DJ (2013) Dynamic analysis of high static low dynamic stiffness vibration isolation mounts. J Sound Vib 332(6): 1437–1455.

[15] Lu ZQ, Wu D, Ding H, Chen LQ (2021) Vibration isolation and energy harvesting integrated in a Stewart platform with high static and low dynamic stiffness. Appl Math Model 89: 249-267.

[16] Xu J, Sun X (2015) A multi-directional vibration isolator based on Quasi-Zero-Stiffness structure and time-delayed active control. Int J Mech Sci 100: 126-135.

[17] Alabuzhev P, Gritchin A, Kim L, Migirenko G, Chon V, Stepanov P (1989) Vibration protecting and measuring system with quasi-zero stiffness. Hemisphere Publishing, New York.

[18] Zhao F, Cao S, Luo Q, Li L, Ji JC (2022) Practical design of the QZS isolator with one pair of oblique bars by considering pre-compression and low-dynamic stiffness. Nonlinear Dyn 108(4): 3313-3330.

[19] Zhao F, Ji JC, Ye K, Luo Q (2021). An innovative quasi-zero stiffness isolator with three pairs of oblique springs. Int J Mech Sci 192: 106093.

[20] Zhao F, Ji JC, Ye K, Luo Q (2020) Increase of quasi-zero stiffness region using two pairs of oblique springs. Mech Syst Signal Process 144: 106975.

[21] Zhang C, He J, Zhou G, Wang K, Xu D, Zhou J (2023) Compliant quasi-zero-stiffness isolator for low-frequency torsional vibration isolation. Mech Mach Theory 181: 105213.

[22] Liu XT, Huang XC, Hua HX (2013) On the characteristics of a quasi-zero stiffness isolator using Euler buckled beam as negative stiffness corrector. J Sound Vib 332(14): 3359-3376.

[23] Ye K, Ji JC (2022) An origami inspired quasi-zero stiffness vibration isolator using a novel truss-spring based stack Miura-ori structure. Mech Syst Signal Process 165: 108383.

[24] Lu ZQ, Gu DH, Ding H, Lacarbonara W, Chen LQ (2020) Nonlinear vibration isolation via a circular ring. Mech Syst Signal Process 136: 106490.

[25] Zeng R, Yin S, Wen G, Zhou J (2022) A non-smooth quasi-zero-stiffness isolator with displacement constraints. Int J Mech Sci 225: 107351.

[26] Wang Y, Li HX, Cheng C, Ding H, Chen LQ (2020) A nonlinear stiffness and nonlinear inertial vibration isolator. J Vib Control 27: 1336-1352.

[27] Jia G, Li B, Huang H, Zhang D (2020) Type synthesis of metamorphic mechanisms with scissor-like linkage based on different kinds of connecting pairs. Mech Mach Theory 151: 103848.

[28] Zhou S, Liu Y, Jiang Z, Ren Z (2022) Nonlinear dynamic behavior of a bio-inspired embedded X-shaped vibration isolation system. Nonlinear Dyn 110(1): 153-175.

[29] Niu MQ, Chen LQ (2022) Analysis of a bio-inspired vibration isolator with a compliant limb-like structure. Mech Syst Signal Process 179: 109348.

[30] Jing X (2022) The X-structure/mechanism approach to beneficial nonlinear design in engineering. Appl Math Mech 43(7): 979-1000.

[31] Ji JC, Luo Q, Ye K (2021) Vibration control based metamaterials and origami structures: A state-of-the-art review. Mech Syst Signal Process 161: 107945.

[32] Yan B, Wang Z, Ma H, Bao H, Wang K, Wu C (2021) A novel lever-type vibration isolator with eddy current damping. J Sound Vib 494: 115862.

[33] Yan B, Yu N, Wang Z, Wu C, Wang S, Zhang W (2022) Lever-type quasi-zero stiffness vibration isolator with magnetic spring. J Sound Vib 527: 116865.

[34] An J, Chen G, Deng X, Xi C, Wang T, He H (2022) Analytical study of a pneumatic quasi-zero-stiffness isolator with mistuned mass. Nonlinear Dyn 108(4): 3297-3312.

[35] Dai W, Li T, Yang J (2022) Energy flow and performance of a nonlinear vibration isolator exploiting geometric nonlinearity by embedding springs in linkages. Acta Mech 233(4): 1663-1687.

[36] Zhang W, Chang ZY, Chen J (2022) Vibration reduction for an asymmetric elastically supported beam coupled to an inertial nonlinear energy sink. J Vib Eng Technol. https://doi.org/10.1007/s42417-022-00666-x

[37] Deng J, Yang J, Jiao S, Long X (2022) Band-stop characteristics of a nonlinear anti-resonant vibration isolator for low-frequency applications. Int J Mech Sci 107914.

[38] Chowdhury S, Banerjee A, Adhikari S (2022) Optimal negative stiffness inertial-amplifier-base-isolators: Exact closed-form expressions. Int J Mech Sci 218: 107044.

[39] Dai W, Shi B, Yang J, Zhu X, Li T (2022) Enhanced suppression of longitudinal vibration transmission in propulsion shaft system using nonlinear tuned mass damper inerter. J Vib Control.

[40] Philip R, Santhosh B, Balaram B (2022) Analytical and numerical investigations on inerter-based NES absorber system with nonlinear damping. Acta Mech 233(11): 4365-4383.

[41] Nie J, Chen L, Huang X, Wei H, Zhang X (2022) Network synthesis design method of nonlinear suspension system with mem-inerter. J Vib Eng Technol. https://doi.org/10.1007/s42417-022-00751-1

[42] Li Y, Jiang JZ, Neild SA (2017) Inerter-based configurations for main-landing-gear shimmy suppression. J Aircr 54(2): 684–693.

[43] Gao H, Wang H, Li J, Mao J, Wang Z (2022) Dynamic behavior and damping enhancement of cable with negative stiffness inerter damper. Int J Mech Sci 235: 107664.

[44] Xue S, Zhang L, Xie L, Zhang R, Kang J (2022) Analytical solutions of inerter-added sliding isolation structures to ground motions. Int J Mech Sci 231: 107568.

[45] Tai YJ, Wang HD, Chen ZQ (2022) Vibration isolation performance and optimization design of a tuned inerter negative stiffness damper. Int J Mech Sci 107948.

[46] Shi B, Dai W, Yang J (2022) Performance analysis of a nonlinear inerter-based vibration isolator with inerter embedded in a linkage mechanism. Nonlinear Dyn 109(2): 419-442.

[47] Dai W, Yang J (2021) Vibration transmission and energy flow of impact oscillators with nonlinear motion constraints created by diamond-shaped linkage mechanism. Int J Mech Sci 194: 106212.

[48] Dai W, Yang J, Shi B (2020) Vibration transmission and power flow in impact oscillators with linear and nonlinear constraints. Int J Mech Sci 168: 105234.

[49] Dai W, Yang J, Wiercigroch M (2022) Vibration energy flow transmission in systems with Coulomb friction. Int J Mech Sci 214: 106932.

[50] Chen Y, Hou L, Chen G, Song H, Lin R, Jin Y, Chen Y (2023) Nonlinear dynamics analysis of a dual-rotor-bearing-casing system based on a modified HB-AFT method. Mech Syst Signal Process 185: 109805.

[51] Krack M, Gross J (2019) Harmonic balance for nonlinear vibration problems. Springer Nature, Switzerland.

[52] Colaïtis Y, Batailly A (2021) The harmonic balance method with arc-length continuation in blade-tip/casing contact problems. J Sound and Vib 502: 116070.